Saturation of Internal Tide Generation over Shallow Supercritical Topography

Jia-Xuan Chang,[a] Jody M. Klymak,[a]

[a] *School of Earth and Ocean Sciences, University of Victoria, Victroia, British Columbia, Canada*

Corresponding author: Jia-Xuan Chang, jiaxuanchang@uvic.ca

ABSTRACT: Understanding the conversion of surface tides into internal tides and resulting turbulence is important for oceanic mixing. This study investigates internal tide generation over shallow supercritical obstacles in flows where $Nh/U_0 \sim O(1)$, with N is background stratification, h obstacle height, and U_0 far-field tidal velocity amplitude. This is particularly relevant in shallow, fjord-like environments where tidal currents become much faster. Previous work has considered the situation where $Nh/U_0 \gg 1$, showing that internal tide generation roughly follows $U_0^2 h^2 N$, and local dissipation follows U_0^3. Here, a faster, linear stratified flow regime is investigated using idealized simulations. Tidal energy conversion follows the U_0^2 power law until crest-top Froude number $Fr_c = U_c/c \approx 1$ (where $U_c = U_0 H/(H-h)$ is the barotropic flow speed at the crest and H is total water depth), beyond which internal tide generation stops increasing (saturates). Radiation saturates and local dissipation no longer grows as quickly as U_0^3. Qualitatively, the fully stratified flow with $Fr_c > 1$ at the crest resembles approach-controlled flow in two layers (Lawrence 1993). Radiation from the crest transitions from relatively linear response with well-defined internal tidal beams to a very non-linear response with diffuse beam as $Fr_c > 1$. However, significant mode-1 internal tides are still radiated into the farfield, contradicting the traditional dichotomy that basins with $Fr_c > 1$ do not generate internal tides (Stigebrandt and Aure 1989). Simulations with realistic or asymmetric stratification exhibit the same general characteristics as constant-stratification simulations. This saturation conversion when $Fr_c > 1$ should be considered when devising wave drag parameterization used in the barotropic tide and global circulation models, especially in fjord regions where large Fr_c are likely to be found.

SIGNIFICANCE STATEMENT: Tidal forcing of stratified flow over a submarine ridge produces internal waves at the tidal frequency and local turbulence. For moderate tides, the energy removed from the surface tide usually scales quadratically with the flow amplitude. Here we show that when the flow speed above the ridge crest exceeds the speed of the lowest internal wave mode the conversion rate stops increasing, and both internal tide radiation and local dissipation no longer increase with stronger forcing. This regime should be taken into account when parameterizing internal tidal drag and mixing, particularly when they are parameterized in shallow seas and fjords.

1. Introduction

Internal tides, known as baroclinic tides, are internal waves with tidal frequencies, generated by the interaction between tides and rugged topographic features. In global models, the mixing induced by internal tides has a significant impact on the ocean state and the Meridional Overturning Circulation in deep-sea regions (Melet et al. 2013), as well as climate (Simmons et al. 2004). In fjord environments, internal tides can be a significant source of the mixing (Bourgault and Kelley 2003; Farmer and Freeland 1983; Klymak and Gregg 2004; Wang 2006; Staalstrøm et al. 2012; Stacey 2005) that can affect estuarine circulation (New et al. 1987) and facilitate deep water renewal (Staalstrøm and Røed 2016).

A substantial portion of global tidal energy (1 TW) undergoes conversion into internal tides within regions characterized by topographic features (Egbert and Ray 2000, 2001). Of particular interest are regions featuring supercritical slopes, where the topographic slope (s) exceeds the slope of the internal tide beam defined by $\alpha = \sqrt{(\omega_0^2 - f^2)/(N^2 - \omega_0^2)}$, where ω_0 the tidal frequency, f the Coriolis frequency, and N the buoyancy frequency. The generation of internal tides at supercritical slopes can be analytically calculated using the knife-edge model (Llewellyn Smith and Young 2003; St. Laurent et al. 2003). Knife-edge theory assumes an infinite slope for predicting internal tide generation at supercritical slopes in a finite deep ocean. Conversion is calculated by

$$F_{knife} = F_0 \sum_{n=1}^{\infty} n^{-1} a_n^2, \tag{1}$$

where

$$F_0 = \frac{1}{2\pi} \rho \frac{\left(\left(N^2 - \omega_0^2\right)\left(\omega_0^2 - f^2\right)\right)^{1/2}}{\omega_0} U_0^2 H^2, \tag{2}$$

n is the number of modes, a_n are the non-dimensional amplitudes of the modes, which depend on $\delta = h/H$ (St. Laurent et al. 2003), h is the obstacle height, H is the total water depth, ρ is seawater density, and U_0 is the tidal current speed. Conversion is proportional to U_0^2, similar to the linear theory of internal tides for subcritical slopes (Bell 1975; Baines 1982).

In fjords, internal tide generation has been estimated using a two-layer linear theory by Stigebrandt (1976); Stigebrandt and Aure (1989). This method assumes the barotropic and baroclinic flows together satisfies the condition of vanishing flow normal to the bottom, thereby obtaining the amplitude of baroclinic tides and equally partitioned kinetic and potential energy. The conversion is as $F_i \approx c_i E \approx \rho h(H-h)/HU_c^2 c_i$, where c_i is the phase speed of the interface wave, E is the energy density and $U_c = U_0 \frac{H}{H-h}$ is the magnitude of barotropic flow at the ridge crest-top. The estimated conversion here is also proportional to squared tidal current but the speed at the ridge crest (U_c).

Our study reveals a novel aspect of stratified internal tide generation at supercritical topography for fjord-like environments, where the relationship between tidal current speed and energy conversion diverges from the quadratic increase as discussed above. The conversion stops growing as U_0^2 once the flow is fast enough so that a crest Froude number defined by $Fr_c = U_c/c_1 \approx 1$. Such conditions are more likely to meet in fjords due to their typically stronger tidal currents and shallower depths, leading to a higher likelihood of internal tide generation saturation compared to the open ocean.

Fully stratified internal tide generation at supercritical obstacles has been studied in the regime of $Nh/U_0 \gg 1$, with particular application to large mid-ocean ridges like Hawaii (Klymak et al. 2008) and Luzon Strait (Alford et al. 2011) and island chains like Palau (Voet et al. 2020). Nh/U_0 has often been interpreted as a nonlinearity parameter (Klymak et al. 2010b; Nikurashin and Ferrari 2010). At this flow regime, there is blocked flow up and downstream of the sill (Baines and Hoinka 1985), and at peak tidal flow, an arrested, breaking non-linear lee wave manifests on the downstream side of the obstacle with a vertical scale of approximately U/N (Klymak et al. 2010a,b; Winters and Armi 2012). The asymmetric flow around the ridge crest can be analogous to the internal hydraulic-controlled flow (Farmer and Armi 1999; Winters and Armi 2013) and the non-linear lee wave can be analogous to the internal hydraulic jump (Legg and Klymak 2008). In this flow regime, local dissipation can be associated with slow internal modes that cannot escape the ridge

($c_n < U_c$), with dissipation essentially following a cubic power law with flow speed (Klymak et al. 2010a).

Most work of internal hydraulics has often focused on two-layer systems. An internal hydraulic-controlled flow occurs when internal Froude number is equal to one at the crest and greater than one downstream (Armi 1986). The flow exhibits lee wave phenomena similar to the deep-ocean case discussed above (Baines and Hoinka 1985; Farmer and Armi 1999) where the crest of the sill is deemed a “critical” hydraulic flow with asymmetric interface across the crest. The lee wave can be thought of as analogous to a downstream hydraulic jump to match the condition where internal Froude number further downstream returns to being less than one. At faster flow speeds the control point moves upstream in what has been termed “approach-controlled flow” (Lawrence 1993). In the subsequent discussion, to avoid confusion, we will use the term “crest-controlled flow” (Lawrence 1993) interchangeably with the commonly employed “hydraulic-controlled flow.” Approach-controlled flow has the internal Froude number greater than one from upstream and over the crest and is thus characterized by relatively flat isopycnals across the ridge crest followed by a sharp plunge downstream of the crest (see Fig. 7b,c of Lawrence 1993). Approach-controlled flow has been observed over coastal sills (Farmer and Denton 1985; Murray et al. 1984), and our simulations not only show the presence of a similar flow pattern when $Fr_c > 1$ but also associate it with the onset of saturation in tidal conversion.

Fjord sill dynamics in two-layer systems have distinguished between “wave basins” and “jet basins” based on Fr_c (Stigebrandt 1976; Stigebrandt and Aure 1989; Stigebrandt 2012). Wave basins with $Fr_c < 1$ are where internal tides are produced, and jet basins with $Fr_c > 1$ are where tidal jets are formed and internal tides were believed to not be possible. However, internal tides have been observed in basins that would be categorized as “jet” basins, such as Loch Etive (Inall et al. 2004; Stashchuk et al. 2007), and this study indicates that even for $Fr_c > 1$ internal tides are generated, although they can be very non-linear.

A two-layer analytical hydraulic model by Arneborg et al. (2017) has indications of internal tide generation saturating as Fr_c approaches or exceeds 1. This study focused on the energy budget at lower Fr_c, and did not discuss the specific details within higher Fr_c regime.

Our study examines the saturation of internal tide generation in stratified flows within fjord-like environments, focusing on the energetics of approach-controlled flow and wave/jet basin classification. Using nonhydrostatic numerical simulations over a two-dimensional Gaussian ridge in a rectangular channel, we maintain constant stratification and exclude rotational effects for simplicity. While recognizing the significance of rotation in subinertial internal tides (Hughes and Klymak 2019), we will address varying stratification in subsequent sections. We present a qualitative analysis of flow characteristics (section 3), a comprehensive evaluation of the baroclinic energy budget, and the criteria for tidal conversion saturation (section 4). Additionally, we study realistic non-linear stratification simplified from Knight Inlet (Klymak and Gregg 2003) and typical estuary asymmetric stratification, which lead to asymmetric lee waves on either side of the sill (Klymak and Gregg 2003). Finally, section 5 discusses hydraulic control conditions and internal tide generation in the regime of $Fr_c > 1$. We consider implications for the parameterization of topographic wave drag in barotropic tide models. These typically employ a linear drag approach, leading to quadratic energy conversion (Arbic et al. 2004; Arbic and Scott 2008; Blakely et al. 2022; Egbert et al. 2004; Jayne and Laurent 2001), which may be unsuitable in regions with strong tidal currents, such as coastal fjords. This is increasingly relevant as rising sea levels, attributed to climate change, are anticipated to induce significant tidal amplitude changes in coastal areas throughout the 21st century, as highlighted by the IPCC (Bindoff et al. 2019).

2. Methods

a. Model configuration

The MITgcm (Marshall et al. 1997) was used to simulate stratified tidal flow over a Gaussian obstacle to investigate internal tide generation and near-ridge dissipation across a range of flow regimes. For the diagnosis of energy budgets, an online barotropic–baroclinic energy decomposition (Kang and Fringer 2012; Klymak et al. 2016; Hughes and Klymak 2019) was used. MITgcm has been demonstrated to accurately capture internal waves, which are crucial in understanding the dynamics of tidal flows over obstacles (Khatiwala 2003; Musgrave et al. 2017).

The simulations were conducted in a 120-km-long, 3-km-wide channel and aimed to loosely resemble the characteristics of Knight Inlet, including a sill height (h) of 140 m, water depth (H) of 200 m, and a sill width of approximately 2.5 km. Knight Inlet was selected for our study due to its reputation as a natural observatory for studying internal tides on supercritical slopes (Cummins et al. 2003, 2006; Farmer and Smith 1980; Farmer and Armi 1999; Klymak and Gregg 2003).

The simulations employed a Cartesian coordinate system (x) centered at the middle of the two-dimensional Gaussian sill. At the scales considered here, the energetics of three-dimensional simulations were identical to those of two-dimensional simulations (see Appendix A), so this paper uses two-dimensional simulations to efficiently cover a wide range of parameters.

The sill profile was defined by the Gaussian function $h = h_0 \exp\frac{-x^2}{a^2}$, with h_0 ranging from 70 to 140 m and $a = 700$, corresponding to a sill width of approximately 2.5 km (see TABLE 1). The lateral resolution of the model was set to 25 m along the channel ($dx_{min} = 25$ m), with grid cells beyond the central region (-15 km $< x <$ 15 km) expanding by 2.7% per cell until reaching a maximum size of $dx_{max} \approx 1225$ m. The vertical resolution was fixed at 5 m, resulting in a total of 40 vertical grid cells. Non-hydrostatic simulations were used because there are differences in the energetics for strong forcing states ($Fr_c = \frac{U_c}{c_1} > 2$) if the hydrostatic approximation is used.

Runs	a	h [m]	H [m]	$N\,[\mathrm{rad\,s^{-1}}]$	U_0 [$\mathrm{cm\,s^{-1}}$]	U_c [$\mathrm{cm\,s^{-1}}$]
base run	700	140	200	0.012	4,8,12,16,24,32,48,64	$\sim 13 \sim 213$
h70		70			8,12,20,36,48,56,64,72,84	$\sim 12 \sim 129$
h110		110			8,12,16,24,32,48,64	$\sim 18 \sim 142$
h120		120			8,12,16,24,32,48,64	$20 \sim 160$
$N/2$		140		0.006	2,4,8,12,16,24,32	$\sim 7 \sim 107$
$2N$		140		0.024	8,16,24,32,48,64,72	$\sim 27 \sim 240$
real N		140		$N_{av} = 0.01138$	4,8,12,16,20,24,32,36	$\sim 13 \sim 120$
asymmetric N		140		$N_{1s} = 0.01$ (upper 100m) , $N_{2s} = 0.005$ (lower 100m) , $N_l = 0.01$	4,8,12,16,20,24,32	$\sim 13 \sim 107$

TABLE 1. Summary of parameters for simulations.

The initial stratification of the model begins with constant N, selecting a value of $1.2\times10^{-2}\ \mathrm{rad\,s^{-1}}$ as base runs to compare to weaker ($6\times10^{-3}\ \mathrm{rad\,s^{-1}}$) and stronger ($2.4\times10^{-2}\ \mathrm{rad\,s^{-1}}$) stratifications (TABLE 1). Realistic non-linear N was also examined and the profile was derived from landward profile near the Knight Inlet sill in summer (Klymak and Gregg 2003) with an average value of approximately $1.138\times10^{-2}\ \mathrm{rad\,s^{-1}}$. Additionally, we conduced experiments with asymmetric stratifications, mimicking the higher stratification in the seaward basin of Knight Inlet (Klymak and Gregg 2003). On the landward side, two layers of constant stratification were employed; on the seaward side, one constant stratification was used throughout the water column (TABLE 1). The density was simulated using a linear equation of state: $\rho = \rho_0\,(1-\alpha_\theta\theta')$, where $\rho_0 = 999.8\ \mathrm{kg\,m^{-3}}$ and $\alpha_\theta = 2\times10^{-4}\ \mathrm{K^{-1}}$.

To drive the tidal currents and density variations in our simulations, nudging boundary conditions were applied at the west and east boundaries. A sponge layer with relaxation timescales of 100 and 1000 s was implemented at the outer and inner edges, respectively, to minimize reflection of internal waves. The tidal forcing was introduced using a sinusoidal function with a period corresponding to the M2 tidal period (T = 44,640 s, so $\omega = \frac{2\pi}{T} \approx 1.4 \times 10^{-4}$ s^{-1}) and a magnitude (U_0) ranging from 4 to 80 cm s^{-1} (TABLE 1). The walls and bottom of the model domain were set to a free-slip condition. The additional bottom friction is incorporated as quadratic bottom drag (with $C_d = 1 \times 10^{-3}$). The time step (dt) of 1.24 s was chosen to satisfy the Courant-Friedrichs-Lewy (CFL) stability criterion, so that $C = u\frac{\Delta t}{\Delta x} < 1$. The simulations were run for a duration of 12 tidal cycles.

Viscosity ν_v and diffusivity κ_v were parameterized based on regions of density overturns (Klymak and Legg 2010) and were assigned low background values ($\kappa_h = \nu_h = 2 \times 10^{-2}$ m^2 s^{-1}, $\kappa_v = \nu_v = 10^{-5}$ m^2 s^{-1}) to maintain numerical stability. The presence of second-order flux-limiting temperature advection scheme (tempAdvScheme = 77; see the MITgcm manual) introduced some numerical diffusivity and dissipation, as noted in Klymak and Legg (2010).

b. Barotropic-baroclinic energy decomposition

Decomposition of barotropic and baroclinic energy (Kang and Fringer 2012) is used to determine the baroclinic energy budgets and dissipation in our simulations. This decomposition is carried out online in our simulations (i.e., not post-processing) to capture the energy in real-time. A depth-integrated, tidally-averaged energy equation is used in the analysis. In a steady, tidally forced system, the barotropic tidal energy is either dissipated in the bottom boundary layer or converted into baroclinic energy. Baroclinic energy can further leave the system as an internal wave energy flux, dissipate in the interior, or dissipate at the bottom boundary layer. The vertically integrated energy budgets becomes

$$\begin{aligned} \frac{1}{T}\Delta\overline{E_0} + \nabla_H \cdot \left\langle \overline{\mathbf{F}_0} \right\rangle &= -\langle \bar{C} \rangle - \langle \overline{\epsilon_0} + D_0 \rangle, \\ \frac{1}{T}\Delta\overline{E'} + \nabla_H \cdot \left\langle \overline{\mathbf{F}'} \right\rangle &= \langle \bar{C} \rangle - \left\langle \overline{\epsilon'} + D' \right\rangle, \end{aligned} \tag{3}$$

where E is tidal energy, F is tidal energy flux, C is conversion from barotropic (BT) to baroclinic (BC) energy, ϵ is turbulence dissipation and D is bottom boundary layer dissipation. Barotropic and baroclinic components are denoted by subscript 0 and prime, respectively. The overbars denote depth integrals, while the angle brackets implicate tidal averages.

We decompose barotropic and baroclinic motions by defining the depth-average properties as barotropic motion for ease of online calculation. This approach can lead to temporary misallocations between barotropic and baroclinic components, especially under conditions of large surface tides, particularly in the estimation of pressure fields because barotropic pressure includes a depth-dependent component due to surface heaving effects (Kelly et al. 2010). However, the misallocated energy is reallocated back after over a distance less than a mode-1 wavelength in our simulations.

In this paper, we focus on the conversion term C, which plays a central role in connecting the energy budgets of barotropic and baroclinic energies, as

$$\overline{C} = \overline{\rho' g W} - \overline{q_z W} + A_{h0} \tag{4}$$

(Kang 2011, Eq. 5.102). The first term is the dominant component of conversion as the linear, hydrostatic part. Here, ρ' represents a density perturbation, and $W(z)$ is the vertical velocity arising from the convergence or divergence of horizontal barotropic flow between the seafloor and depth z. The second term represents the nonhydrostatic contribution to the conversion, q is the nonhydrostatic part of the pressure. The third component is the non-linear term as

$$A_{h0} = \rho_0 (U \nabla_H \cdot \overline{\mathbf{u}'_H u'} + V \nabla_H \cdot \overline{\mathbf{u}'_H v'}). \tag{5}$$

Following conversion, baroclinic energy undergoes two processes: local dissipation, which we integrate over a 10-km wide control volume centered on the ridge, and propagation out of the system. The component that leaves the system is described by the depth-integrated baroclinic flux, denoted as $\overline{F'} = \overline{u'p'} + \overline{uE'}$, where p' and u' are the baroclinic components, and E' is baroclinic energy density (Kang 2011, Eq. 5.102). We neglect the diffusive components of F' as they are negligible.

The dissipation at the bottom boundary layer is divided into barotropic and baroclinic components, represented as

$$\begin{aligned} D_0 &= \rho_0 C_d \mathbf{u}_H (uU + vV), \\ D' &= \rho_0 C_d \mathbf{u}_H (uu' + vv' + w^2), \end{aligned} \tag{6}$$

where uppercase, lowercase, and primed velocities refer to the barotropic, complete, and baroclinic components, respectively, and the subscript H pertains to the horizontal component. This decomposition is non-unique, so we follow the convention used by Carter et al. (2008), Kang and Fringer (2012) and Hughes and Klymak (2019) for consistency.

Turbulent dissipation due to vertical shear ϵ_v is obtained from the modeled vertical viscosity as

$$\epsilon'_v = \rho_0 \nu_v \left(\left(\frac{\partial u}{\partial z} \right)^2 + \left(\frac{\partial v}{\partial z} \right)^2 \right), \tag{7}$$

and horizontal dissipation is calculated as

$$\epsilon'_h = \rho_0 \nu_H \left(\nabla_H \mathbf{u}'_H \cdot \nabla_H \mathbf{u}'_H \right). \tag{8}$$

3. Phenomenology: increasing tidal forcing

Under weaker tidal forcing condition ($U_0 = 8$ cm s^{-1}, FIG. 1), where $Nh/U_0 \sim 21 \gg 1$, the flow exhibits non-linear trapped internal lee waves (Klymak et al. 2010b; Winters and Armi 2012; Legg 2021) akin to crest-controlled flow (Lawrence 1993) in two layers, as discussed in the introduction. Lee waves are formed downstream of the ridge crest during both flood and ebb tides, deepen as tides strengthen (FIG. 1b-c,f-g), and collapse before slack tide (FIG. 1d-e,h-a). Breaking lee waves, similar to downstream hydraulic jumps, are a source of local turbulence. Blocked flow is observed both upstream and downstream of the sill. Above the blocked layer, an accelerated flow initiates and later transitions to nearly horizontal flow several kilometers downstream (at about 60 m in depth in FIG. 1c,d,g,h).

Simulation with stronger tidal forcing ($U_0 = 24$ cm s^{-1}, FIG. 2), where Nh/U_0 drops to 7, the flow becomes more non-linear. Isopycnals exhibit increased non-linear structures, such as bores and seesaw patterns. Lee waves with bigger amplitude (FIG. 2c,g) than those in FIG. 1c,g form during both ebb and flood tides. However, the amplification of lee wave amplitude is less than threefold the size seen in FIG. 1c,g, contrary to the expected scaling based on the vertical scale of U/N. Breaking lee waves are not only amplified also trigger numerous trailing waves or bores. There is less upstream blocking, and more isopycnals are able to climb up the crest.

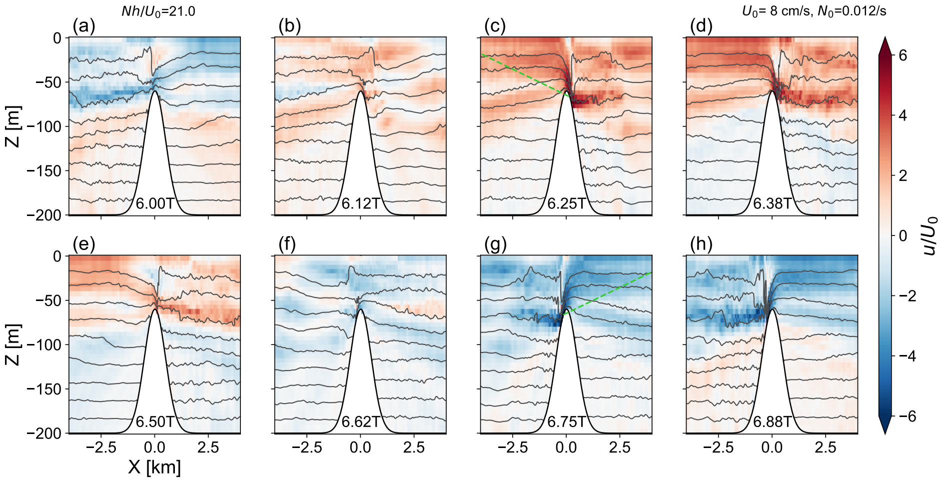

Fig. 1. Snapshots of velocity and density over a tidal cycle when $Nh/U_0 = 21$, where $U_0 = 8$ cm s^{-1}, $N = 1.2 \times 10^{-2}$ rad s^{-1}, and $h = 140$ m. (a,e) is during slack tide and (e,g) is during peak tides. Green dash curves in (c,g) are the slope of internal tides beam. Tidal non-linear lee waves are generated on both flood and ebb tides and the flow near ridge crest resembles crest-controlled flow with asymmetric interfaces.

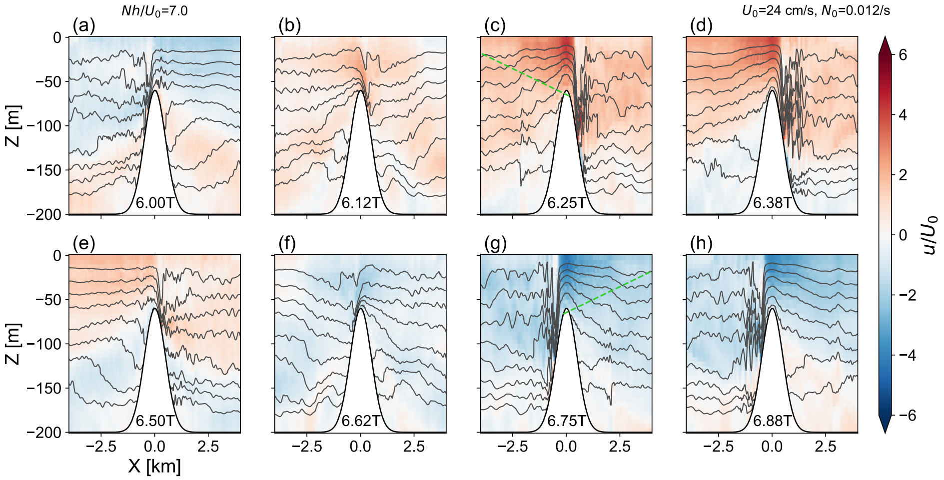

Fig. 2. Snapshots of velocity and density over a tidal cycle when $Nh/U_0 = 7$, where $U_0 = 24$ cm s^{-1}, $N = 1.2 \times 10^{-2}$ rad s^{-1}, and $h = 140$ m. (a,e) is during slack tide and (e,g) is during peak tides. Green dash curves in (c,g) are the slope of internal tides beam. This flow does not resemble crest-controlled flow, but is qualitatively very similar to approach-controlled flow (Lawrence 1993).

More importantly, the nature of the control at the crest changes between the weaker and stronger forcing examples (fig. 3). Under weaker forcing, isopycnals show an asymmetry across the ridge, indicative of crest-controlled flow. In contrast, with stronger forcing, isopycnals are relatively flat

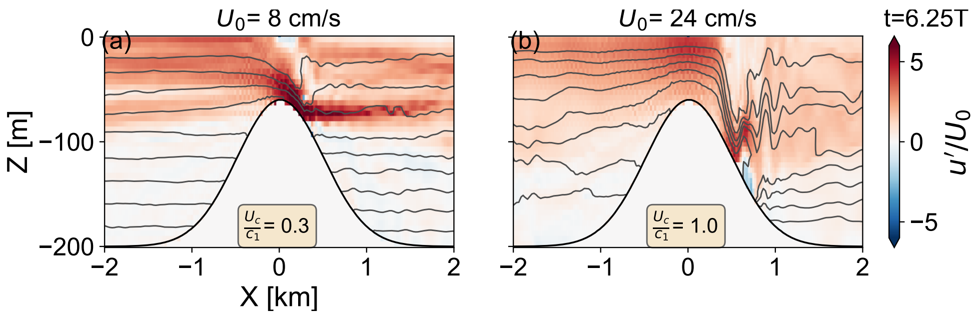

FIG. 3. The control of the flow changes as tidal forcing increases. The detail snapshots of velocity and density from FIG. 1c and FIG. 2c during peak flood tide. The isopycnals transition from (a) asymmetric (i.e., the plunge starts from upstream towards downstream) to (b) symmetric (i.e. the isopycnals are relatively flat above the crest with the symmetry axis at $X = 0$) across the ridge crest. Note the described symmetry is only very near the ridge top within 500 m away from the crest. Asymmetric/symmetric flow patterns resemble to those of crest/approach-controlled flow.

and symmetric across the ridge before plunging abruptly downstream, characteristics that resemble approach-controlled flow in two layer (Lawrence 1993). In the weak forcing scenario, the flow accelerates attached to the crest, following a horizontal jet that extends downstream. In contrast, under strong forcing, the flow becomes concentrated above the crest near the surface, with the accelerated flow not extending as far downstream. This more diffuse jet just below the crest on the downstream side is likely due to an undular jump. It is important to note that here is 2D simulation, and the undular bores may not be as prominent in a three-dimensional flow.

The flow undergoes a transition from crest-controlled to approach-controlled flow as tidal forcing is increased (FIG. 4). Weaker tidal forcing exhibits crest-controlled flow (FIG. 4a-d), while stronger forcing has approach-controlled flow (FIG. 4e-h), with a transition at about $U_0 = 24\,\mathrm{cm\,s^{-1}}$ ($Nh/U_0 = 10.5$). For the strongest flow, the hydraulic jumps is almost pushed downstream off the topography. The hydraulic jump also becomes more undular as the forcing is increased. The transition from crest-controlled to approach-controlled occurs when the flow speed at the top of the crest ($U_c = U(H-h)/H$) is approximately equal to the mode-1 phase speed in the deep part of the channel ($c_1 = NH/\pi$).

We test this with lower ridges ($h/H = 0.35$) and observe similar patterns of transition from crest-controlled to approach-controlled flow (FIG. 5), indicating the change of control is not exclusive to high ridges. The transition for this lower ridge occurs at distinct forcing, $U_0 = 56$ cm s^{-1}, and

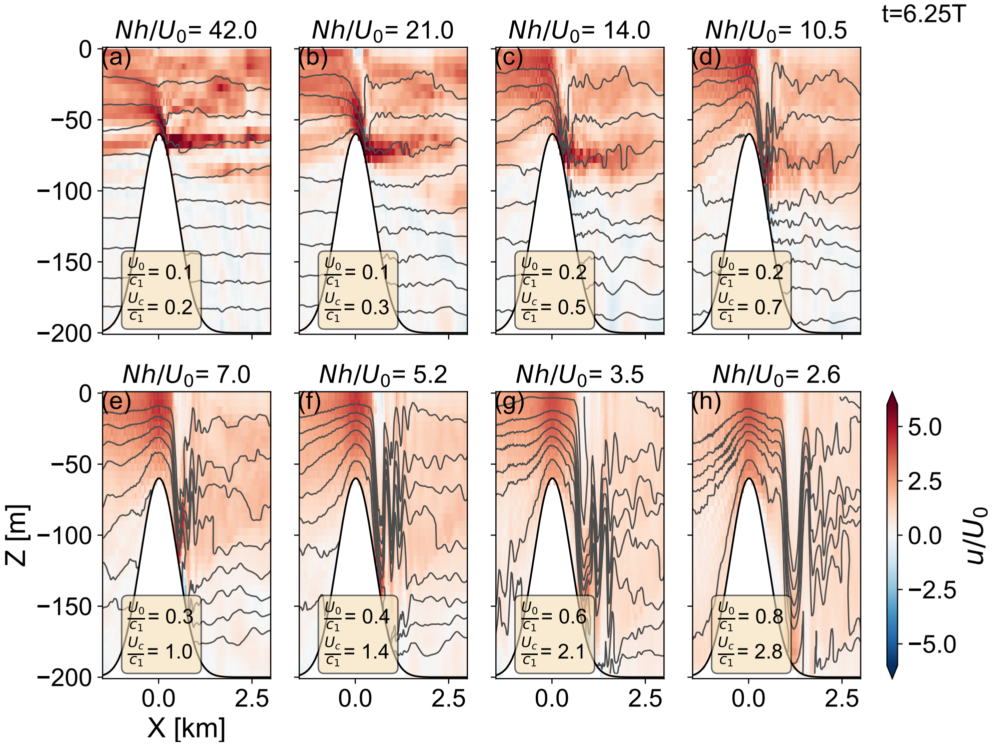

FIG. 4. Snapshots of velocity and density at peak flood tide as tidal forcing U_0 increases from 4 to 64 $\mathrm{cm\,s^{-1}}$ for $h = 140$ m, $N = 1.2\times10^{-2}$ $\mathrm{rad\,s^{-1}}$. Nh/U_0, U_0/c_1 and U_c/c_1 also are indicated. Flow resembles two stages, from (a-c) crest-controlled flow to (d-h) approach-controlled flow. Transition is at about $U_0 = 24$ $\mathrm{cm\,s^{-1}}$ ($Nh/U_0 = 10.5$ and $Fr_c = U_c/c_1 = 0.7$).

different $Nh/U_0 = 1.5$ (FIG. 5e). Notably, the crest-top flow speed U_c also approximates mode-1 phase speed c_1 when the transition occurs. The crest-top Froude number $Fr_c = U_c/c_1 \sim 1$ criterion for detecting the control changes seems to be reinforced by testing different ridge heights.

Simulations with the stratification doubled and halved show the same change in response at crest-top Froude number (Fr_c) of approximately 1. While plots of these flow changes are not included in this subsection, the corresponding energy budgets are discussed below.

4. Baroclinic energy budgets

In this section, we examine the energetics of the flow as it transitions from crest-controlled to approach-controlled by increasing the tidal forcing as shown in the previous section. We do this by calculating the rate that energy is put into the baroclinic tide (or the conversion term), and

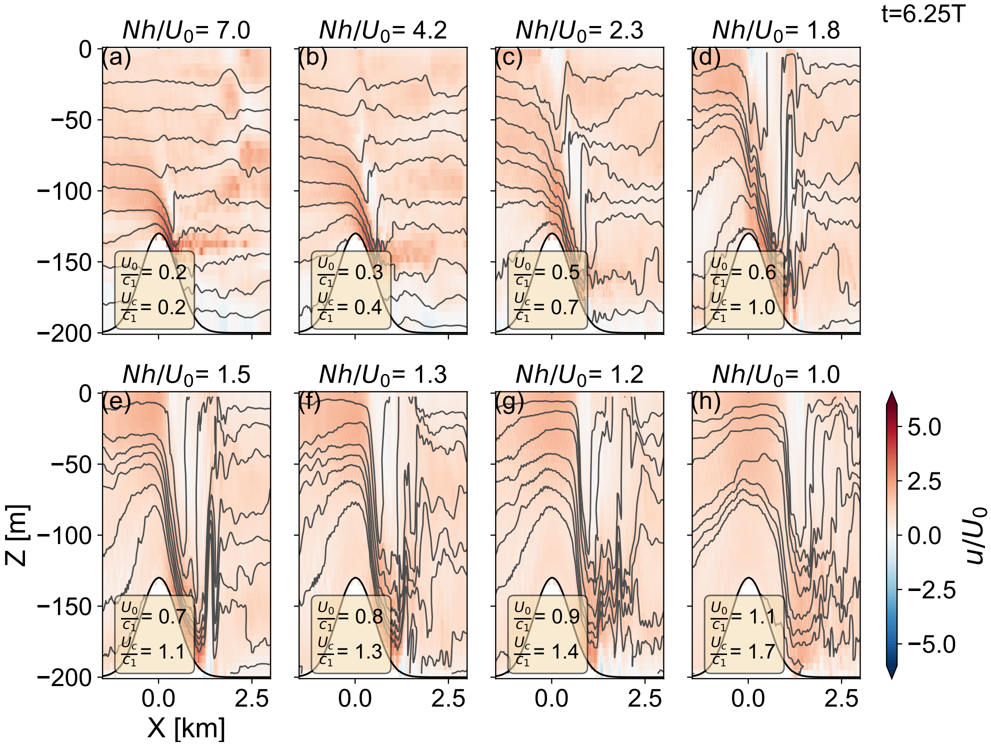

FIG. 5. Snapshots of velocity and density at peak flood tide as tidal forcing U_0 increases from 8 to 84 $\mathrm{cm\,s^{-1}}$ for $h = 70$ m, $N = 1.2\times10^{-2}$ $\mathrm{rad\,s^{-1}}$. Nh/U_0, U_0/c_1 and U_c/c_1 also are indicated. Flow also resembles two stages in this lower ridge, (a-d) crest-controlled flow and (e-h) approach-controlled flow. Transition is at about $U_0 = 56$ $\mathrm{cm\,s^{-1}}$ ($Nh/U_0 = 1.5$ and $Fr_c = U_c/c_1 = 1.1$)

assess the fraction that is locally dissipated due to turbulence versus the fraction that radiates away as baroclinic waves, where "locally" is a 10-km long control volume centered on the obstacle (equation (3)). The results at weaker forcing follow previous literature, but as forcing increases and $Fr_c > 1$ the conversion and radiation terms in the energy budget saturate.

a. Dependence on tidal amplitude

The saturation of barotropic to baroclinic conversion can be seen in a pair of simulation suites that have the same stratification ($N = 1.2\times10^{-2}$ $\mathrm{rad\,s^{-1}}$), ridge heights of 140 or 70 m, and a variety of velocity forcing from 0.06 to 0.84 $\mathrm{m\,s^{-1}}$ (FIG. 6). The knife edge prediction for the conversion rate scales as U_0^2 (black lines). The simulated conversion, $\langle\bar{C}\rangle$ (FIG. 6, green curves), follows the knife-edge prediction at small velocities, but saturates as the velocities increase in both simulation suites. For the lower ridge, the conversion even experiences a decline.

Baroclinic radiation from the 10-km control volume, $\nabla \cdot \langle \bar{F'} \rangle$ (FIG. 6, orange curves), follows a trend similar to the conversion, shifting from a nearly quadratic increase under weak tidal forcing and plateauing as tidal forcing strengthens. The radiation falls off somewhat more strongly because dissipation continues to increase for both topographic heights. The vertical dissipation rate, $\langle \bar{\epsilon_v} \rangle$ (FIG. 6, red curves), dominates the dissipation terms, and increases slightly faster than cubically with tidal forcing and then less quickly when the baroclinic conversion saturates. For the lower ridge (FIG. 6b, d) dissipation even drops as the saturation condition is reached.

The enhanced turbulent dissipation at strong tidal forcing reduces the stratification near the ridge, but only by 15% (FIG. 7e,f). This is not sufficient to account for the reduced conversion, as indicated the modified knife-edge model (in the linear relationship with stratification, gray lines).

The fraction of energy dissipated is approximately 10% for the weaker flows, and increases to over 40% of the conversion for stronger flows, and exceeds the fraction that radiates (FIG. 6c,d). These fractions resembles the energy distribution observed in various locations: Knight Inlet, where 2/3 of energy is radiated away, and 1/3 is dissipated near the sill (Klymak and Gregg 2004); Hawaiian Ridge, 15% (Klymak et al. 2006); Mendocino Escarpment, 28% (Musgrave et al. 2016); Luzon Strait, 40% (Alford et al. 2015), but differs from Oslo Fjord, where it ranges from 60 – 90% (Staalstrøm et al. 2015). In mixing parameterization of global models, the fraction of energy dissipated locally is often chosen to be 0.3 (St. Laurent et al. 2002).

The horizontal dissipation $\langle \bar{\epsilon_h} \rangle$ and bottom friction dissipation $\langle D' \rangle$ have minimal contributions to the local dissipation (FIG. 6a,b, purple and blue curves), with quadratic growth (i.e., similar slope with black lines) before saturation and the nearly parallel trend with vertical dissipation after saturation. Our energy budget has a residual of approximately 10 to 15% of the conversion term in all scenarios (FIG. 6c,d, gray x), potentially arising from numerical dissipation (Klymak and Legg 2010), consistent with other studies employing a similar methodology (Hughes and Klymak 2019).

b. Saturation criteria

Given the parameters of the problem, h, H, N, and U_0, we seek a parameter that collapses the response of the conversion so we can predict when saturation will be reached for a given

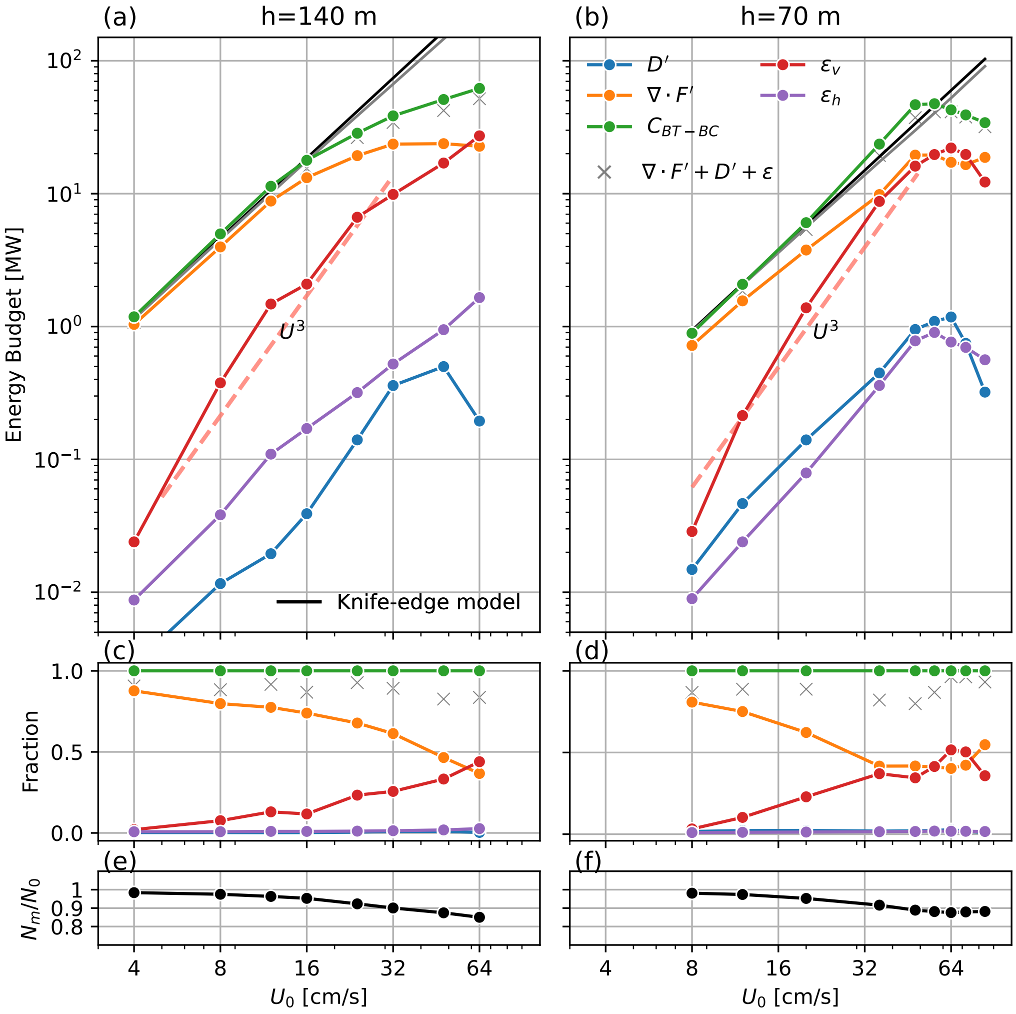

FIG. 6. Left panel is $h = 140$ m and right panal is $h = 70$ m. (a,b) Baroclinic energy budgets within ±5 km for $N = 1.2 \times 10^{-3}$ rad s^{-1} and (c,d) the fraction of the baroclinic energy budgets to conversion versus the tidal forcing U_0. Green curves are barotropic-baroclinic energy conversion $\langle \bar{C} \rangle$, orange ones are the divergence of baroclinic energy flux $\nabla \cdot \langle \bar{F}' \rangle$ (or baroclinic radiation), red ones are vertical dissipation $\langle \bar{\epsilon}_v \rangle$, purple ones are horizontal dissipation $\langle \bar{\epsilon}_h \rangle$, blue ones are bottom friction $\langle D' \rangle$. Black lines are knife-edge prediction in a square relationship to U_0 (St. Laurent et al. 2003). (e,f) are the scaled mean stratification near the ridge (away from sill 2 to 5 km). Modified knife-edge solution by the mean stratification in (a,b) as gray lines. A plateau is shown in both conversion and radiation when strong tidal forcing, what we called conversion saturation.

flow. Barotropic to baroclinic conversion is calculated with different ridge heights and background stratification (FIG. 7). Conversion saturation occurs across all tested simulations, as each curve is initially linear, then progressively bends (FIG. 7a). However, the specific point at when saturation occurs depends on N and h.

To compare different simulation scenarios, we normalized each simulation by the expected conversion from the knife edge model, which predicts internal tide generation on supercritical ridges as discussed in section 1. After normalizing each simulation by the expected conversion from the knife edge model, the most non-dimensional similarity of the saturation was achieved by using Fr_c (FIG. 7d). Other normalizations (FIG. 7b,c) showed a wider spread, particularly for different obstacle heights, indicating that the barotropic speed over the obstacle was an important factor. The saturation curves are not perfect, even when normalizing by Fr_c, and the shortest obstacle, $h = 70$ m in particular has an apparent resonance near $Fr_c = 1$. However, most of the simulations start to saturate at about $Fr_c \approx 0.5 - 0.7$.

The onset of saturation corresponds with the qualitative occurrence of approach-controlled flow, as indicated by their Nh/U_0 and Fr_c values presented in our plots (FIG. 4 and FIG. 5). For instance, for the 140-m tall ridge, the simulation with $Fr_c = 0.7$ ($Nh/U_0 = 10.5$, FIG. 4d) is approximately when the conversion starts to saturate (FIG. 7b,d). In that simulation, and the ones with stronger barotropic forcing, the isopycnals over the top of the ridge can be seen to become flat, with a sharp drop on the downstream side. The same phenomena happens for the shorter ridge, but at a higher velocity (FIG. 5e, $Nh/U_0 = 1.5$, and FIG. 7b,d).

The full suite of simulations has relatively similar responses for the radiation and dissipation across the range of Fr_c (FIG. 8), with the fraction of dissipation increasing as Fr_c increases (FIG. 8d). The radiation (FIG. 8a) response follows a growth pattern proportional to U_0^2 when tidal forcing is weak, reaching a saturation point as $Fr_c > 1$. Dissipation (FIG. 8b) shows a power-law dependence on U_0. For higher ridges (blue curves), the dissipation transitions from a faster-than-expected cubic decay to a nearly square behavior when $Fr_c > 1$. For lower ridges (the pink to purple curves), the dissipation reaches nearly constant when $Fr_c > 1$. The curves with the same stratification (pink to purple curves and middle blue one) do not collapse as in radiation (FIG. 8a), with the lowest ridge having proportionally larger dissipation, likely due to its larger absolute value of U_0^3.

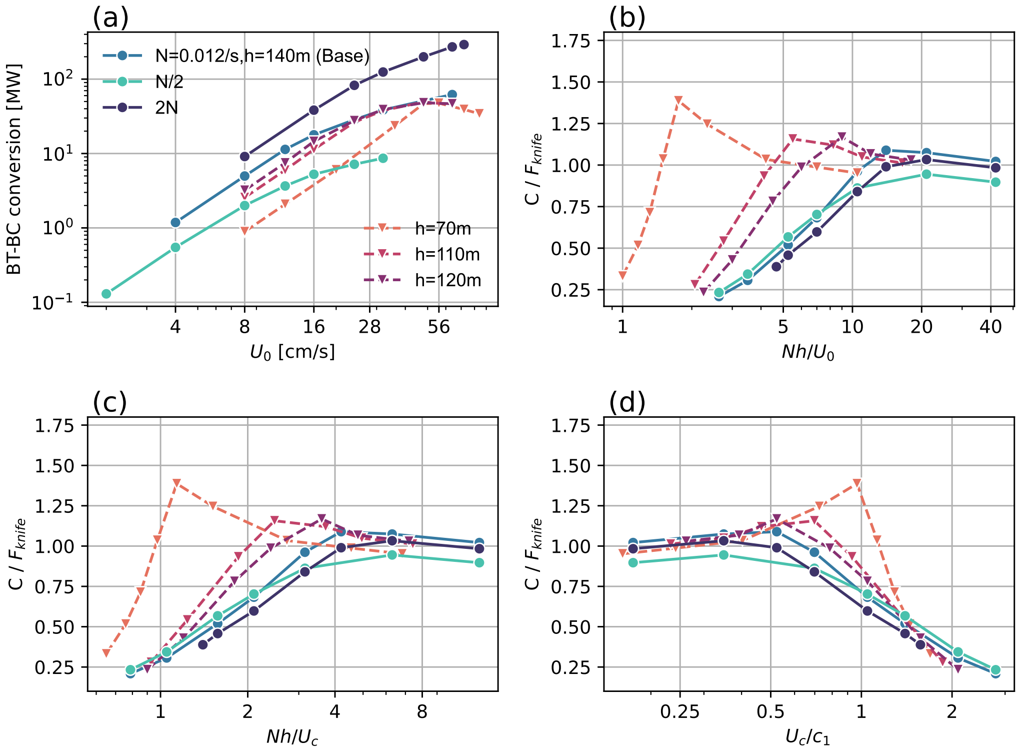

Fig. 7. (a) Barotropic-baroclinic conversion versus the tidal forcing U_0 and normalized conversion by knife-edge prediction versus (b) Nh/U_0, (c) Nh/U_c, and (d) $Fr_c = \frac{U_c}{c_1}$, where U_c is the barotropic flow speed at crest and c_1 is the internal tide mode 1 speed, in different experiments. The blue series represents experiments with differing stratification intensities, with darker shades of blue indicating increased stratification. Conversely, the pink to purple spectrum represents experiments with varying ridge heights, where deeper hues correspond to higher ridges. The best collapse of the saturation was achieved using Fr_c while most of the simulations start to saturate at about $Fr_c \approx 0.5-0.7$.

c. Realistic stratification

Having shown the saturation phenomenon in the constant stratification simulations, we now demonstrate that the same phenomena occurs for realistic non-linear stratifications. First, we use the simplified summer landward density profile from the Knight Inlet observation (Klymak and Gregg 2003). The density profile exhibits a sharp pycnocline and a weak ($\sim 2\times10^{-3}$ $\mathrm{rad\,s^{-1}}$) and uniform bottom stratification within about the bottom 50 m, with an average stratification of 1.138×10^{-2} $\mathrm{rad\,s^{-1}}$ and mode-1 speed of 0.8471 $\mathrm{m\,s^{-1}}$.

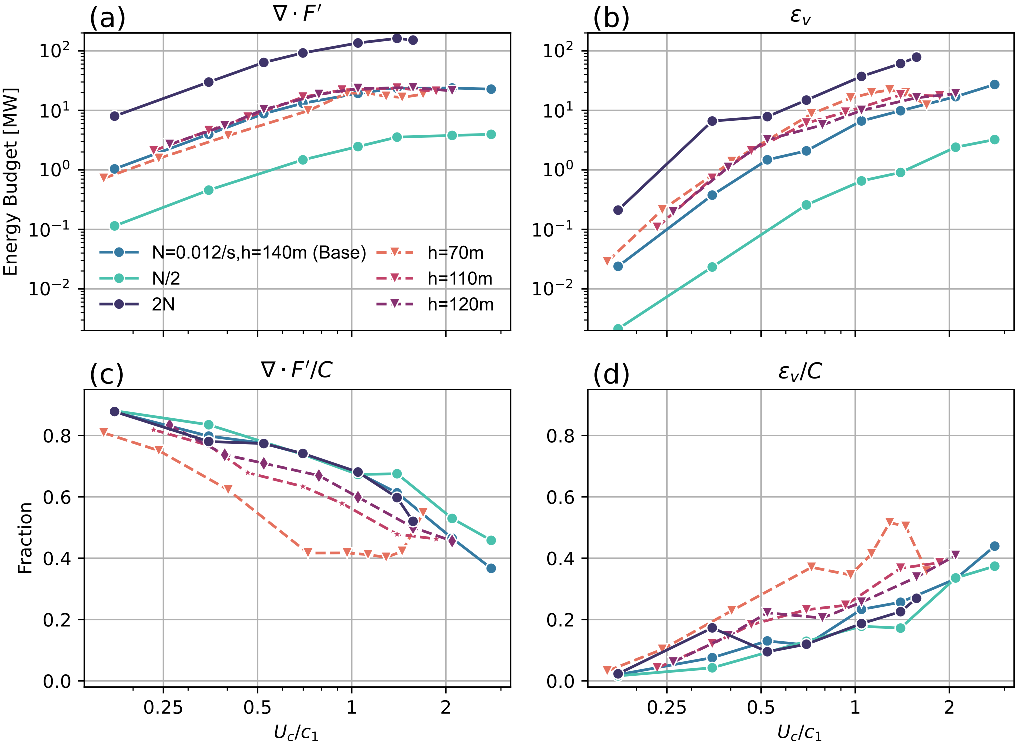

Fig. 8. (a) Baroclinic radiation and (c) its fraction to conversion, and (b) vertical dissipation and (d) its fraction to conversion versus $Fr_c = \frac{U_c}{c_1}$, where U_c is the barotropic flow speed at crest and c_1 is the internal tide mode 1 speed, in different experiments. The blue series represents experiments with differing stratification intensities, with darker shades of blue indicating increased stratification. Conversely, the pink to purple spectrum represents experiments with varying ridge heights, where deeper hues correspond to higher ridges.

The changes in the control of the flow observed in realistic stratification experiments are the same as those observed in constant stratification experiments (Fig. 9). Non-linear trapped internal lee waves are seen when the tidal forcing is weaker ($Fr_c < 1$). When $Fr_c > 1$, the flow becomes symmetric over the sill, indicate of approach-controlled flow (Fig. 9g,h). The sharp isopycnal drops of Fig. 9h and Fig. 4f, both exhibiting the same Fr_c, are similar. Isopycnals show more overturns on both the upstream and downstream sides than the one with constant N. The upstream blocking is easier to overcome than constant N, probably due to the weaker stratification at the bottom.

These simulations exhibit the same saturation of energy conversion (green curve, Fig. 10) as constant stratification simulations. The knife-edge model under the realistic stratification requires consideration of WKB-stretching for h_{WKB} and U_{0WKB}. Accordingly, $(H-h)_{wkb} = \int_{-H+h}^{0} N dz/N_{av} \approx$ 122.06 m, so $\delta_{wkb} = h_{wkb}/H = 0.3897$. Next, $F_{knife}/F_0 = \sum_{n=1}^{\infty} n^{-1} a_n^2$, where a_n are nondi-

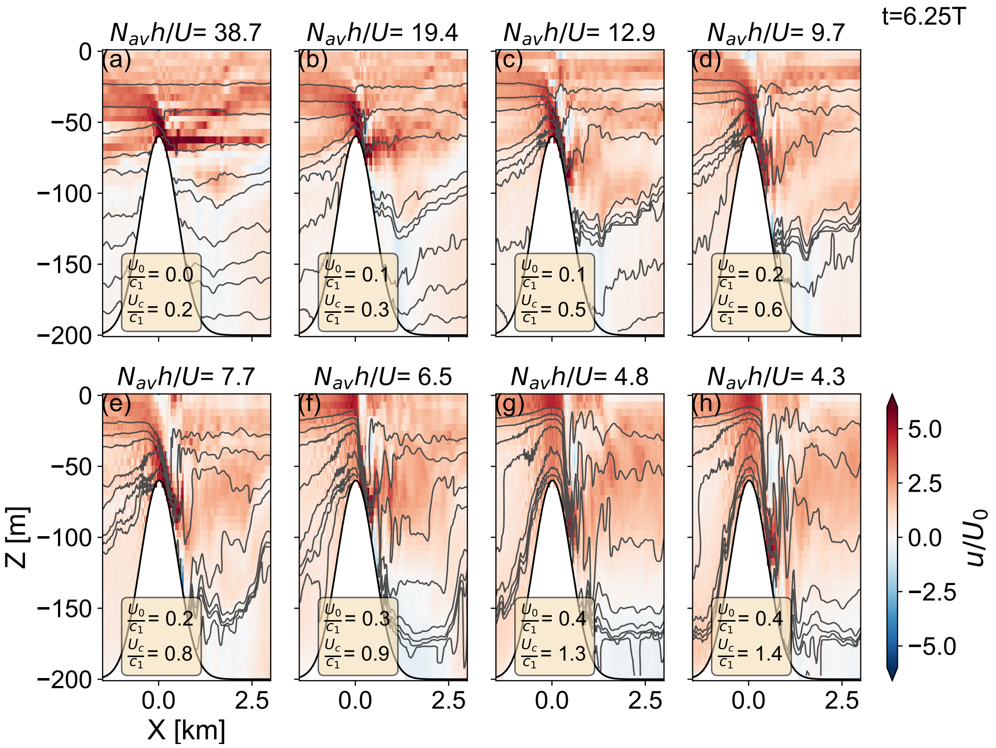

FIG. 9. Snapshots of velocity and density with a realistic, non-constant stratification at flood tide as tidal forcing U_0 increases from 4 to 36 cm s^{-1} for $h = 140$ m. Initial stratification N is the simplified N profile from Knight Inlet (Klymak and Gregg 2003). Contours are non-uniformly spaced in density but uniformly spaced in depths (20 m per layer) on initial density so that the displacements of the isopycnal are easy to observe. Nh/U_0, U_0/c_1 and U_c/c_1 also are indicated. The control of the flow also changes in this realistic N experiments, resembling (a-e) crest-controlled and (f-h) approach-controlled flow. Transition is at about $U_0 = 24$ cm s^{-1} ($Nh/U_0 = 6.5$ and $Fr_c = U_c/c_1 = 0.9$)

mensional coefficients of each mode determined by δ (St. Laurent et al. 2003). Consequently, $F_{knife}/F_0 = 0.802$. From $F_0 = \frac{\pi}{2}\rho U_{0wkb}^2 H^2 \frac{((N_{av}^2-\omega^2)(\omega^2-f^2))^{0.5}}{\omega} L_y$ and $U_{0wkb} = U_0(N_{av}/N)^{0.5}$, we can obtain F_{knife}. The conversion (green curve) closely aligns with the knife-edge model when $Fr_c < 1$; , saturation is observed for higher Fr_c in the realistic simulations. The results of baroclinic radiation (orange curve) and dissipation (red curve) are similar to those of constant stratification, with both showing saturation at $Fr_c > 1$, but the realistic stratification exhibits slower growth of radiation when $Fr_c < 1$ due to greater dissipation, manifesting as more zigzags in isopycnals (FIG. 9).

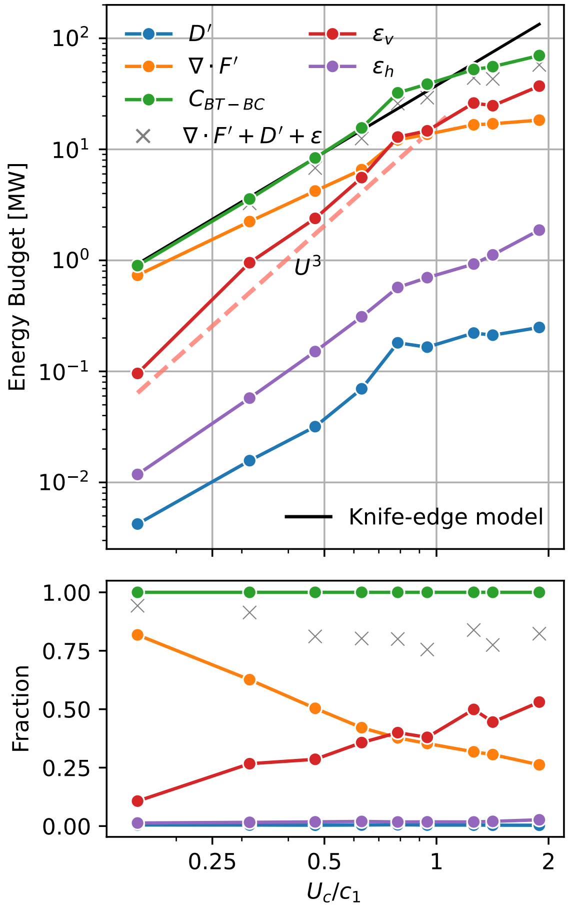

Fig. 10. Baroclinic energy budgets within ±5 km and the fraction of the baroclinic energy budgets to conversion for $h = 140$ m with a realistic, non-constant stratification versus the tidal forcing U_0. The colors indicating different energy components are the same as those used in fig. 6. Black lines are knife-edge prediction in a square relationship to U_0 (St. Laurent et al. 2003). Conversion saturation also occurs at $Fr_c \sim 1$ in realistic stratification.

d. Asymmetrical stratification

A similar saturation of the energy terms occurs when the stratification is unequal in the basins on either side of the obstacle. This situation is typical of estuaries, where denser seawater flows into the estuary and less dense freshwater flows from the landward basin. The size of the lee waves formed either side of the sill is shown to be different under such asymmetric stratification (Klymak and Gregg 2003). We use a constant N of 1×10^{-2} rad s^{-1} on the seaward side and a two layer constant N profile on the landward side with $N = 1 \times 10^{-2}$ rad s^{-1} in the upper 100 m and $N = 5 \times 10^{-3}$ rad s^{-1} in the lower 100 m. Seaward side density is always greater than landward side density at every depth level. We calculate the energy budget still in the 10-km long control volume centered on the obstacle, even acknowledging baroclinic energy behaves differently on either side of the sill. We use the density of the seaward side for potential energy calculations in MITgcm to avoid potential energy changes caused by intruding water on the landward side. The knife-edge model is also computed using the seaward side stratification.

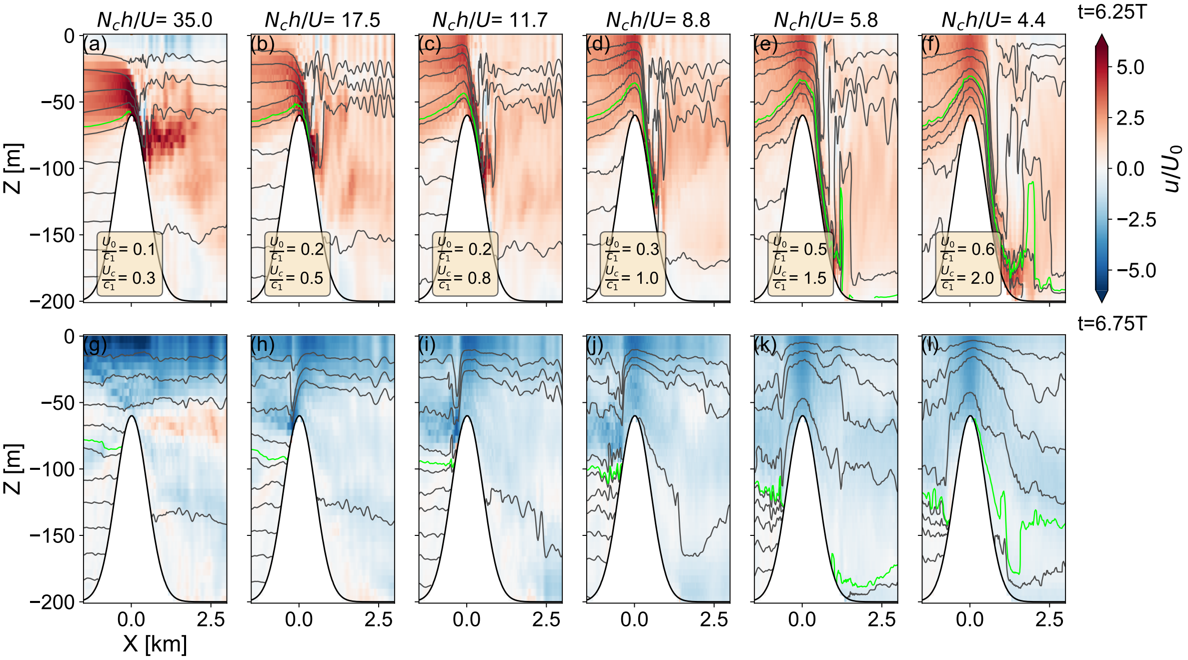

FIG. 11. Snapshots of velocity and density from the simulation with the unequal stratifications on either side of the obstacle at flood (upper) and ebb (lower) tide as tidal forcing increases from 4 to 32 $\mathrm{cm\,s^{-1}}$ for h = 140 m. Asymmetric stratification is typical of estuaries: seaward with denser water (left side), and landward with less dense freshwater (right side). Contours are non-uniformly spaced in density but uniformly spaced in depths (20 m per layer) on initial seaward density. Green curves are the densest isopycnals for the landward side. Nh/U_0, U_0/c_1 and U_c/c_1 also are indicated. The control of the flow also can be seen with this specific stratification; resembling (a,b,g,h) crest-controlled and (c-f,i-l) approach-controlled flow. Transition is at about $U_0 = 24\ \mathrm{cm\,s^{-1}}$ ($Nh/U_0 = 6.5$ and $Fr_c = U_c/c_1 = 0.9$)

Despite the asymmetric response of flow on either side of the sill during flood and ebb tides due to asymmetric stratification, the transition of flow control (FIG. 11) and energy saturation (FIG. 12) still occurs at $Fr_c \sim 1$. The asymmetry is consistent with Klymak and Gregg (2003), where lee waves reach deeper on the side with weaker stratification. Denser water intrudes landward (FIG. 11b-f), indicated by the green curves. The conversion closely aligns with the knife-edge model when $Fr_c < 0.8$ but is slightly lower due to the choice of the seaward side for calculations (green curves, FIG. 12). Afterwards, the conversion and baroclinic radiation start to saturate (orange curves), similar to the constant and realistic stratification experiments. Vertical dissipation (red curve) shows an overall nearly quadratic trend.

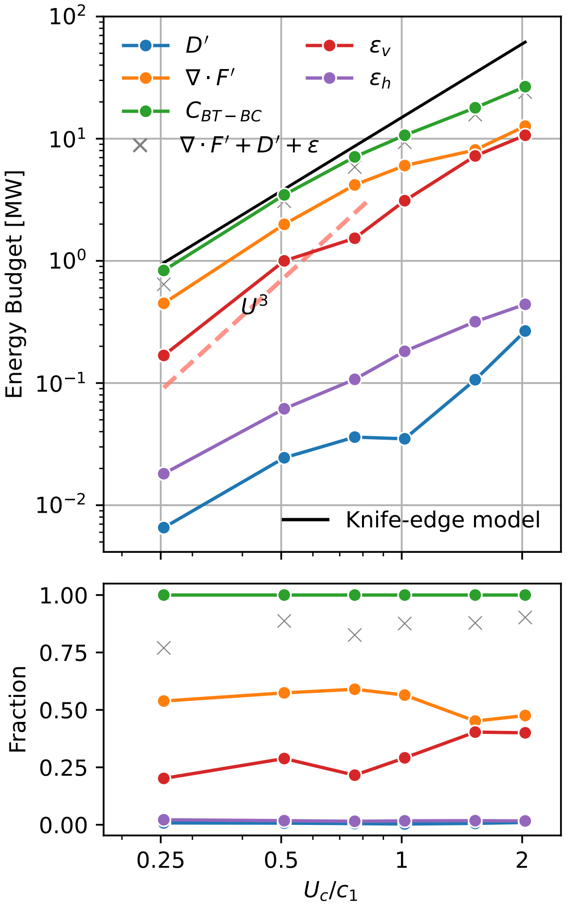

FIG. 12. Baroclinic energy budgets within ± 5km for $h = 140$ m with the unequal stratifications on either side of the obstacle versus the tidal forcing U_0. The colors indicating different energy components are the same as those used in FIG. 6. Black lines are knife-edge prediction in a square relationship to U_0 (St. Laurent et al. 2003). Conversion saturation also occurs at $Fr_c \sim 1$ in asymmetric stratification.

5. Summary and discussion

As flow velocity increases, in a strongly non-linear parameter space, Nh/U_0 declines from $O(10)$ to $O(1)$, altering the flow dynamics near ridges from typical lee waves to a distinctive pattern with symmetric flow near the ridge crest, followed by sharply rapid isopycnal plunging downstream and dramatic hydraulic jumps further downstream. This pattern resembles "approach-controlled flow." Upstream blocking may be entirely overcome at higher flow velocities. From an energy perspective, the conversion from tidal to internal tide energy no longer adheres to knife-edge theory, rather saturating with flow velocity instead of quadratic scaling when $Fr_c = U_c/c_1 > 1$. This affects the subsequent baroclinic energy radiation and local dissipation, with radiation saturating and local dissipation growing at a slower rate than cubic to flow velocity, still leading to an increasing dissipation ratio of up to 40%. All of these features can be seen in the simulations with constant, realistic, asymmetric stratification.

a. Evaluating hydraulic controls

In our investigation of tidal dynamics, we identified a correlation between the crest Froude number (Fr_c) nearing or exceeding 1 and the emergence of flow characteristics resembling approach-controlled flow, which coincides with the saturation of tidal energy conversion. This subsection further examines the hydraulic conditions using the two-layer composite Froude number (G), $G^2 = F_1^2 + F_2^2 - eF_1^2F_2^2$, where $e = (\rho_2 - \rho_1)/\rho_2$, $F_1 = u_2/g'h_1$, $F_2 = u_2/g'h_2$, and u is layer depth-averaged flow velocity, and the undisturbed composite Froude number (G_0), given

$$G_0 = \frac{q}{(g'r(1-r)H^3)^{0.5}},$$

where q is the flow rate and $r = q_2/q$ and q_2 is the flow rate of lower layer (Lawrence 1993), to deepen our understanding of their interrelations and implications for energy dynamics. These values are depicted in FIG. 13 e-h. Note G_0 is meaningful far away from the ridge, representing the undisturbed state. A limitation of this method is the transformation from a continuously stratified flow to a two-layer system, which proved sensitive to the choice of layer interface. This sensitivity affects the computed G value by influencing flow rate, thickness of the layer, and reduced density.

Despite the limitation, a clear pattern emerged: when the selected isopycnal was near the level of the jet—characterized by strong flow over the ridge, G curves mirrored those resembling of crest-controlled flow (FIG. 13a,c), characterized by a notable peak (G_{max}) at the crest (orange curves in FIG. 13e,g). Conversely, G curves to those resembling approach-controlled flow (FIG. 13b,d) presented a wider spatial extent near the ridge crest, with G values surpassing the value away from ridge (orange curves in FIG. 13f,h). We observed the greatest G_{max} when the interface was nearest to the jet, leading us to select this interface for representing this analysis.

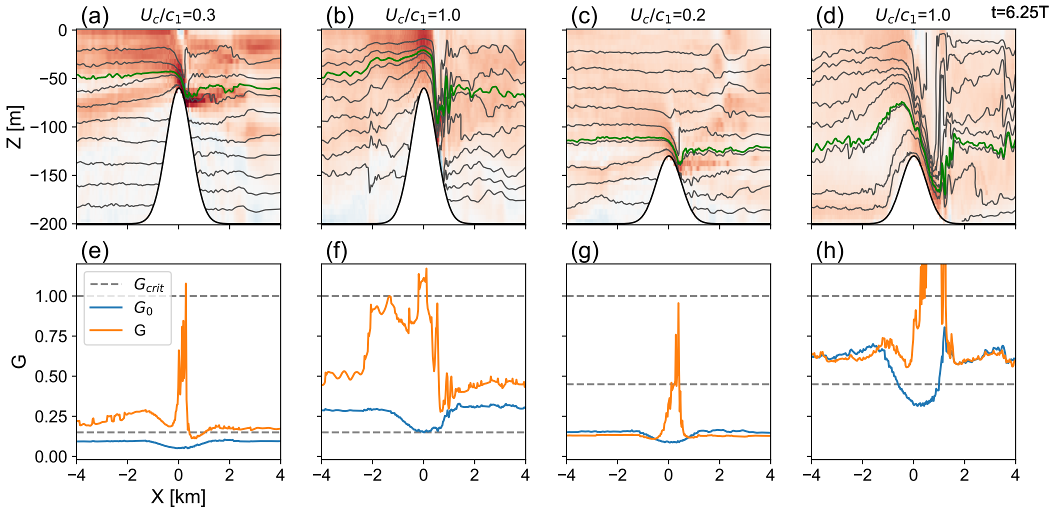

FIG. 13. Snapshots of velocity and density at flood tide at (a) $U_c/c_1 = 0.3$, $h = 140$ m, (b) $U_c/c_1 = 1.0$, $h = 140$ m, (c) $U_c/c_1 = 0.2$, $h = 70$m, (d) $U_c/c_1 = 1.0$, $h = 70$ m. The green curves are the selected two-layer interface in order to calculate their corresponding composite internal Froude number G (orange curves), the undisturbed composite Froude number G_0 (blue curves, Lawrence 1993) and the critical values for approach-controlled flow and supercritical flow (gray dash lines).

Lawrence (1993) classification method, which compares G_0 with critical G_0 values (as shown by the blue and dashed lines in FIG. 13 e-h, respectively), proved generally consistent with the flow behaviors and our Fr_c-based analysis. In scenarios where Fr_c was significantly less than 1, G_0 remained below the critical threshold indicative of crest-controlled flow. For cases around $Fr_c \sim 1$, G_0 exceeded the critical value, suggesting approach-controlled flow conditions.

For our case of the lower ridge with $Fr_c \sim 1$ (FIG. 13 d), the flow does not yet display the perfect alignment with the typical patterns of approach-controlled flow, which we surmise might become more apparent at $Fr_c \sim 1.1 - 1.3$ (FIG. 5e,f). However, at $Fr_c \sim 1$, the G_0 method already shows values exceeding the critical G_0, suggesting a consistency with the onset of tidal energy conversion saturation. Therefore, while Fr_c is a quite robust criteria for identifying saturation, G_0 computation could provide an additional means, even though the question of why changes in hydraulic control conditions lead to tidal energy saturation remains. This is particularly relevant when observation of internal tides near lower ridges might not clearly indicate approach-controlled characteristics; in such cases, both Fr_c and G_0 could be helpful in discerning whether conversion saturation has occurred.

b. Internal tide generation in the regime of $Fr_c > 1$

In the fjord-related literature, it has been believed that basins with $Fr_c > 1$, often referred to as tidal jet basins, do not generate internal tides (Stigebrandt 1976; Stigebrandt and Aure 1989). This subsection revisits this regime, proposing that internal tides can indeed form under these conditions, as evidenced by near-field flow pattern similarities with others observation, which also observed internal tides in the $Fr_c > 1$ regime, and far-field wave propagation in our study.

Our analysis of near-field flow patterns, although not directly indicative of internal tides, shows similarities to those observed in studies where internal tides were detected in the far-field (Inall et al. 2004, 2005; Stashchuk et al. 2007). These characteristics include a jet attached along the slope that flattens downstream, similar to the typical lee waves generated when the flow is crest-controlled (Fig. 8 of Stashchuk et al. (2007) v.s. FIG. 9b at 50 m $< z <$ 80 m and $0 < x <\sim 2$ km). As the flow strengthens (Fig. 9 of Stashchuk et al. (2007)), the isopycnals above the ridge crest become flatter, with surface flow intensifying, and then abruptly plunging downstream until reaching the ridge surface. The hydraulic jump further downstream is also evident. After the jump, the jet continues horizontally. These similarities align with the characteristics of approach-controlled flow, which are very analogous to our simulation results (FIG. 9f at 0 m $< z <$ 80 m and $0 < x < 0.5$ km).

In the far-field, our simulations directly indicate that internal tides radiate, though their character becomes more and more non-linear (FIG. 14). The presence of mode-1 waves extending away from the ridge at high Fr_c values, aligning with the concept that internal tides can indeed be generated in such flow as $Fr_c > 1$. Inall et al. (2004) and Stashchuk et al. (2007) reported mode-1 internal tides downstream, ranging from 2 km to 15 km when $Fr_c > 1$ in Loch Etive. In our case, the perturbation with tidal frequency are shown across all the temporal snapshots in FIG. 14 even to a downstream

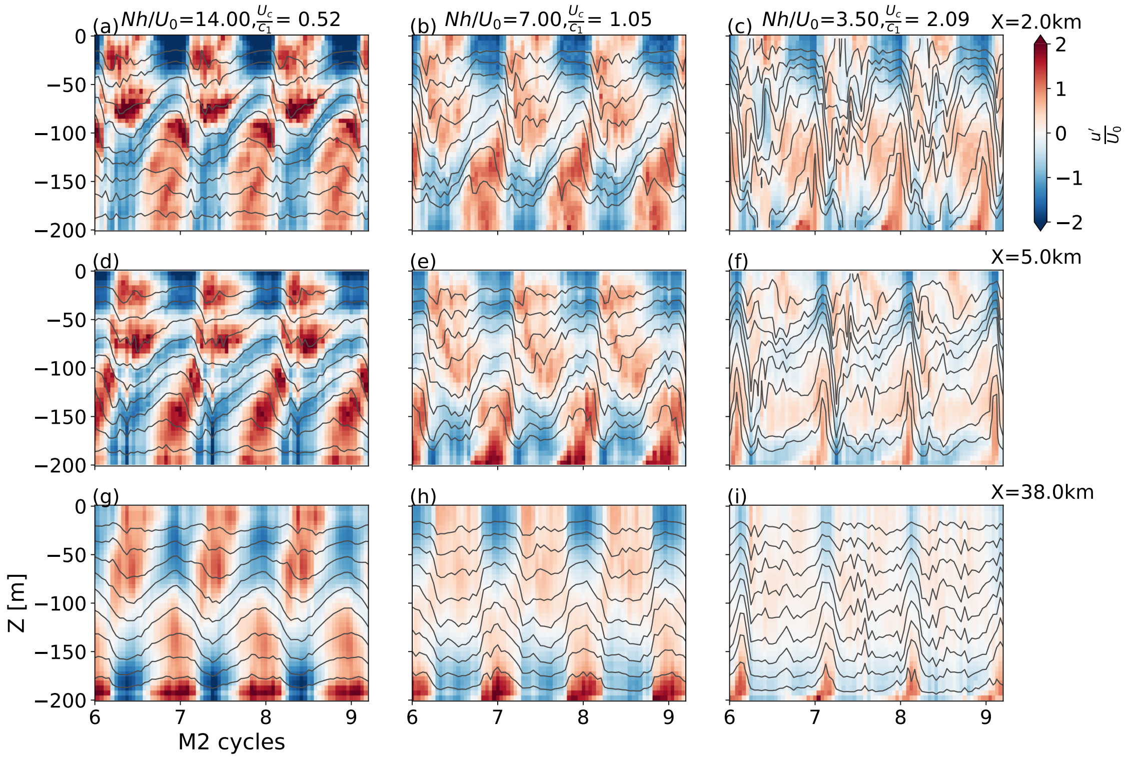

FIG. 14. Temporal snapshots of the baroclinic flow (a,d,g) $Fr = 0.52$, (b,e,h) $Fr = 1.05$ and (c,f,i) $Fr = 2.09$ at (a,b,c) $X = 2$ km, (d,e,f) $X = 5$ km, (g,h,i) $X = 38$ km. The simulations are based on the same setup as the previous base runs, with modifications to achieve higher spatial resolution in the far-field region. The resolution increases from $dx_{min} = 25$ m at -35 km $< X <$ 35 km, expanding by 2.37% per cell until reaching a maximum size of approximately 600 m. The perturbation with tidal frequency is shown in all cases even when $Fr_c > 1$ and far away from the sill, suggesting internal tides are still generated when $Fr_c > 1$.

distance of 38 km with $Fr_c \sim 2$ (FIG. 14i). As Fr_c increased, there is a transition in the wave train from a more linear and sinusoidal form to a non-linear pattern. Comparing our results to Loch Etive observations at 2 km downstream (Fig 10 in Stashchuk et al. 2007), both the observations and our simulations identified short steep troughs and longer flatter crests at subsurface depths, as depicted in FIG. 14b,c.

These observations challenge the traditional dichotomy of tidal jet and wave basins based on Fr_c. Contrary to previous classifications, the consistency between our simulations and the far-field suggests that supercritical flow conditions do not inhibit the generation of internal tides.

Further into the far-field, we observe a few interesting patterns when $Fr_c \sim 2$ (FIG. 15c): distinct phase relationships emerge between the off-ridge (i.e., the background tides move away the ridge)

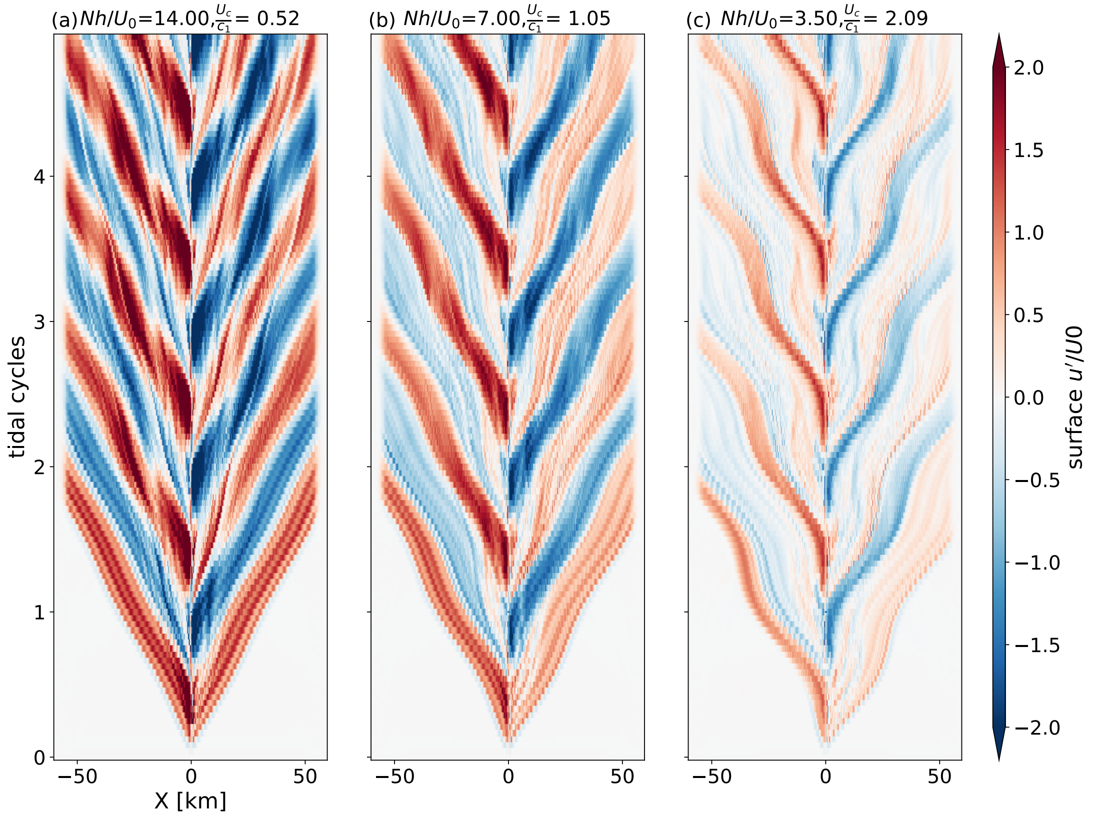

FIG. 15. Hovmuller diagram of the surface baroclinic flow (a) $Fr = 0.52$, (b) $Fr = 1.05$ and (c) $Fr = 2.09$. The simulations are based on the same setup as the previous base runs, with modifications to achieve higher spatial resolution in the far-field region. The resolution increases from $dx_{min} = 25$ m at -35 km $< X <$ 35 km, expanding by 2.37% per cell until reaching a maximum size of approximately 600 m.

	Energy [MW]	C	$\nabla \cdot F'$	ϵ	D'	$\nabla \cdot F' + \epsilon + D'$
$Fr = 0.52$	5km	11.63	9.07 (78 %)	1.32 (11 %)	0.02 (0.1 %)	10.41 (89.5 %)
	38km	11.53	7.82 (68 %)	1.49 (13 %)	0.97(8 %)	10.28 (89.1 %)
	$\Delta_{(38km-5km)}$	-0.09	-1.25	+0.16	+0.95	-0.13
$Fr = 1.05$	5km	29.27	20.09 (69 %)	6.58 (22 %)	0.11 (0.4 %)	26.78 (91.5 %)
	38km	28.77	16.06 (56 %)	7.60 (26 %)	2.52 (9 %)	26.18 (91.0 %)
	$\Delta_{(38km-5km)}$	-0.51	-4.03	+1.02	+2.41	-0.60
$Fr = 2.09$	5km	54.64	26.18 (48 %)	21.32 (39 %)	0.54 (1 %)	48.05 (87.9 %)
	38km	54.35	19.98 (37 %)	24.18 (44 %)	3.74 (7 %)	47.90 (88.1 %)
	$\Delta_{(38km-5km)}$	-0.29	-6.21	+2.86	+3.20	-0.15

TABLE 2. Baroclinic energy budgets at $x = 5$ km and $x = 38$ km for $Fr = 0.52$, $Fr = 1.05$, and $Fr = 2.09$.

and on-ridge (i.e., the background tides move towards the ridge) components as internal tides propagate outward. Specifically, on the right-hand side of the ridge, the phase with westward velocity in the upper water column tends to exhibit a shorter wavelength compared to the one with eastward velocity (FIG. 15c and FIG. 16c,f,i). Additionally, the phase propagation speed varies significantly between flood and ebb tides (FIG. 15c). These patterns indicate a distinctive and noteworthy hydrodynamic mechanism in regimes where $Fr_c > 1$, in contrast to $Fr_c < 1$. A full exploration of these mechanisms, however, lies beyond the scope of our study.

Nonlinearity significantly increases as $Fr_c > 1$, characterised by a more diffuse tidal beam and enormous zigzags in the isopycnals (FIG. 16b,c). While we may expect there may not be much internal waves left at $Fr_c \sim 2$, the tidally-averaged baroclinic energy flux still shows approximately 37% radiating away at 38 km (orange curves in FIG. 16l and TABLE 2), indicative of considerable waves propagating even at this distance when $Fr_c \sim 2$. These flux are mostly mode-1 waves by observing one zero-crossing in FIG. 14 and FIG. 16 and modal energy flux distribution (not shown). As mentioned in section 2, the energy flux along the channel (orange curves in FIG. 16l) is shown temporary misallocations due to the way we decomposed the barotropic and baroclinic components (Kelly et al. 2010), it relocates back over one mode-1 wavelength. The outstanding question of where these mode-1 waves dissipate remains in this strong non-linear scenario.

The evidence presented strongly suggests that the regime where $Fr_c > 1$ not only supports the generation of internal tides but also introduces complexities in their formation and propagation that needs further investigation.

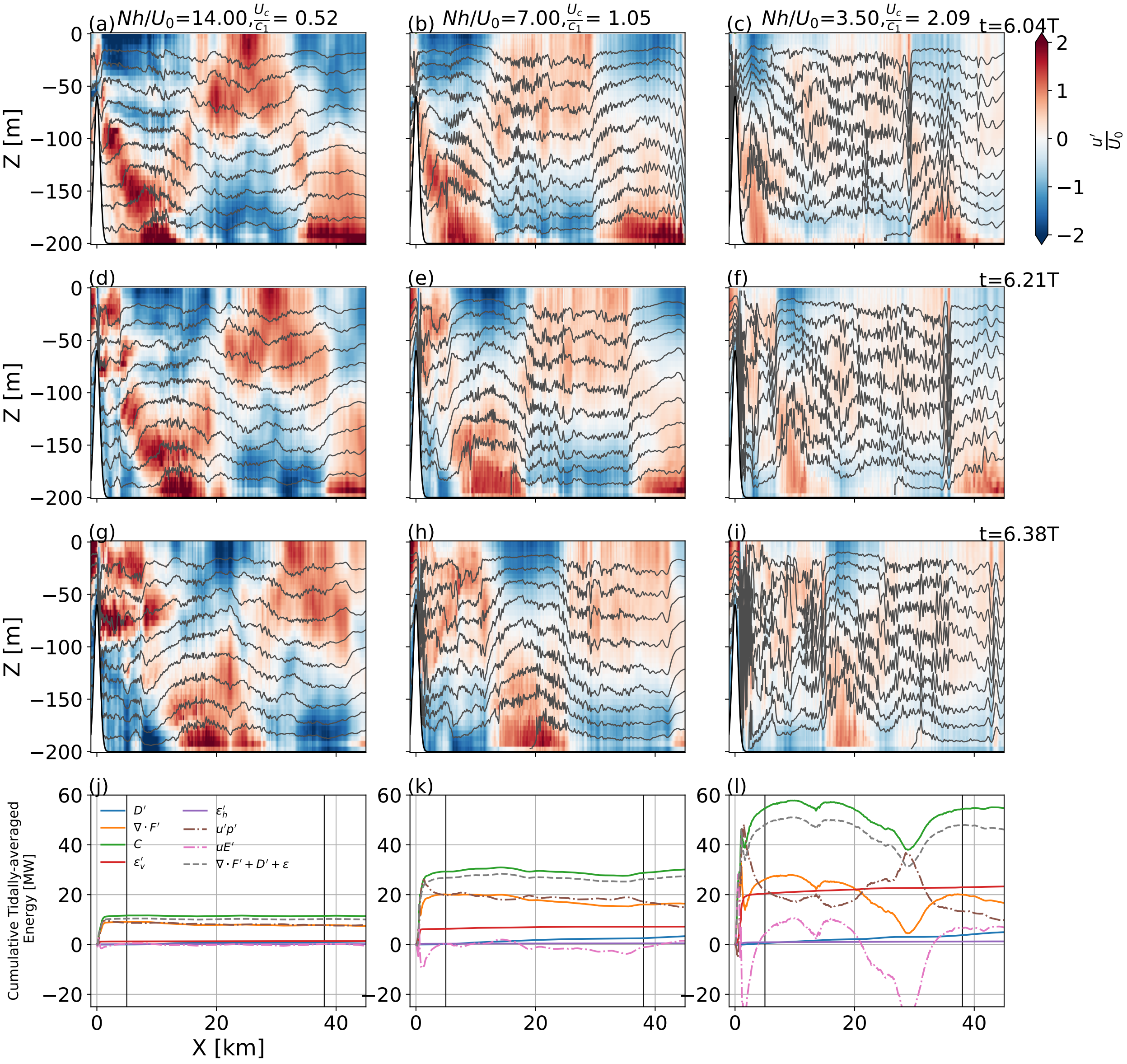

Fig. 16. Snapshots of the baroclinic flow (a,d,g) $Fr = 0.52$, (b,e,h) $Fr = 1.05$ and (c,f,i) $Fr = 2.09$ at (a,b,c) t=6.04T, (d,e,f) t=6.21T, (g,h,i) t=6.38 T. Tidally-averaged cumulative energy budgets for (j) $Fr = 0.52$, (k) $Fr = 1.05$ and (l) $Fr = 2.09$ with colors representing different energy components as in Fig. 6. Additionally, two components in baroclinic energy flux are shown: $\overline{u'p'}$ (dashed brown) and $\overline{uE'}$ (dashed pink). Vertical lines are the reference position for calculate energy budgets in Table 2. Nonlinearity significantly increases as $Fr_c > 1$, characterised by more diffusive tidal beam and many zigzags in the isopycnals. The tidally-averaged baroclinic energy flux (orange curves in (l)) still shows approximately 37% radiating away at 38 km (Table 2), indicative of considerable waves propagating even at this distance when $Fr_c \sim 2$.

c. Concluding remarks

Knife-edge theory provides accurate predictions for tidal conversion on supercritical slopes, based on a power law that exhibits a quadratic relationship with U_0 and a linear relationship with h and N. However, as flow velocities increase beyond $Fr_c > 1$, a deviation from this quadratic scaling is observed — a saturation of energy conversion.

Our findings align with two-layer model of Arneborg et al. (2017), indicating a reduction in normalized conversion as Fr_c approaches 1 (their Figure 9,10). We utilized the knife-edge model as a reference for conversion, in contrast to their use of Stigebrandt and Aure (1989)'s model for tidal loss at a fjord sill, both of which account for the squared tidal current speed. This implies that their solutions also show a ceased growth in tidal conversion in relation to U_0^2 near $Fr_c \sim 1$. The fact that the two-layer flow computations also suggest such saturation indicates this saturation may be intrinsic to flows with $Fr_c > 1$.

We present evidence that there exists a regime between crest-controlled flow ($Fr_c = 1$ at the crest) and fully supercritical flow ($Fr = U_0/c_1 > 1$ everywhere) where energy continues to be transferred from barotropic to baroclinic motion, albeit at a diminishing rate. This transfer may persist until reaching supercritical flow, at which point a reversion to predominantly barotropic motion is expected. However, the behavior of the system under fully supercritical conditions lies beyond the scope of our study.

As tidal forcing increases in the tidal non-linear lee wave regime ($Nh/U_0 \gg 1$), the scaling relationships between energy conversion and turbulent dissipation must reconcile; otherwise, dissipation, scaling with U_0^3 , would exceed conversion, scaling with U_0^2, which is physically unreasonable. This indicates that a new scaling relationship or regime must emerge to maintain physical consistency at higher forcing. This study delineates the limit of that regime, providing a framework that can guide future research in tidal energy dynamics.

Due to the requirement for wave drag parameterization in forward, global, barotropic tide models, current models primarily utilize a linear topographic wave drag parameterization of U, and h and N within a tensor C for representing dissipative forces arising from tidal conversion (Buijsman et al. 2015; Griffiths and Peltier 2009; Green and Nycander 2013). Accordingly, the relationship between energy conversion and U is quadratic. There is a need for improvement, especially in cases involving supercritical slopes, shelf and coastal regions (Buijsman et al. 2015; Stammer et al.

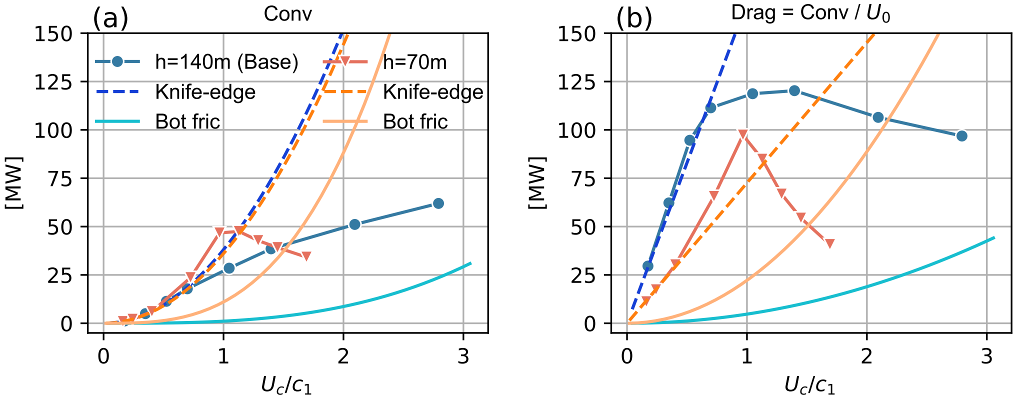

FIG. 17. (a) Conversion and (b) drag are the function of U_c/c_1. Blues curves are the energy and drag of $h = 140$ m and oranges are $h = 70$ m. Solid curves with markers are the our simulation results, dash curves are knife-edge model and solid curves are the quadratic drag $C_d u^2$ and dissipation $C_d u^3$ due to bottom friction.

2014; Sulzbach et al. 2021), where the relative errors may reach 16% (Stammer et al. 2014). Prior research has concentrated on tuning the C tensor, often leaving the linear U component unadjusted. As an example, Green and Nycander (2013) introduced a threshold for the C tensor as a means of mitigating errors. Our study reveals that when $Fr_c > 1$, the conversion reaches saturation. For higher ridges, it approaches nearly linearity (blue circle marker curves, FIG. 17a), while for lower ridges, it approximates a constant value (orange triangle marker curves, FIG. 17a). Drag (conversion divided by U_0) for higher ridges remains about constant (blue circle marker curves, FIG. 17b), whereas for lower ridges, it follows nearly power-law decay with an exponent of -1 (orange triangle marker curves, FIG. 17b). If tidal forcing continues to increase, bottom friction quadratic drag (solid curves, FIG. 17)) can take over at $Fr_c = 1.5$ for $h = 70$ m, and at $Fr_c \sim 4$ for $h = 140$ m. In summary, from $Fr_c < 1$, linear wave drag is effective; from $Fr_c > 1$ up to a certain threshold dependent on ridge heights, wave drag should transition to a power-law decay to U_0 or no dependence to U_0; and when $Fr_c \gg 1$, bottom friction quadratic drag becomes dominant. This suggests a method for improving wave drag parameterization, at least in shallow water, by introducing a threshold for U where $Fr_c > 1$, deviating from a linear wave drag.

Acknowledgments. This work was funded by NSERC Discovery Grant 327920-2006. Computations were performed on the Cedar supercomputer, supported by Digital Research Alliance of Canada (`https://alliancecan.ca/en`). Ann Gargett provided numerous helpful suggestions on this paper.

Data availability statement. All files required to set up and configure representative simulations using MITgcm are available in a Github repository (`https://github.com/jiaxuanchang/TallRid_nonhydr`).

APPENDIX A

Validation of Two-dimensional Simulations

In the three-dimensional simulations, all settings mirror those of the two-dimensional experiments, with the exception of the y-direction resolution ($dy = 25$ m, $ny = 120$), the Coriolis parameter $f = 10^{-4}$ s $^{-1}$ corresponds to a latitude of approximately 50^o, and hydrostatic mode. There is a significant degree of similarity between the two-dimensional and three-dimensional models, particularly with regard to tidal conversion and radiation. Although the two-dimensional simulations exhibit more vertical dissipation since there is no extensive horizontal dissipation, the combined vertical and horizontal dissipations in both dimensions are comparable. In spite of the visual differences on plots, the alignment in bottom friction is supported by its negligible magnitude.

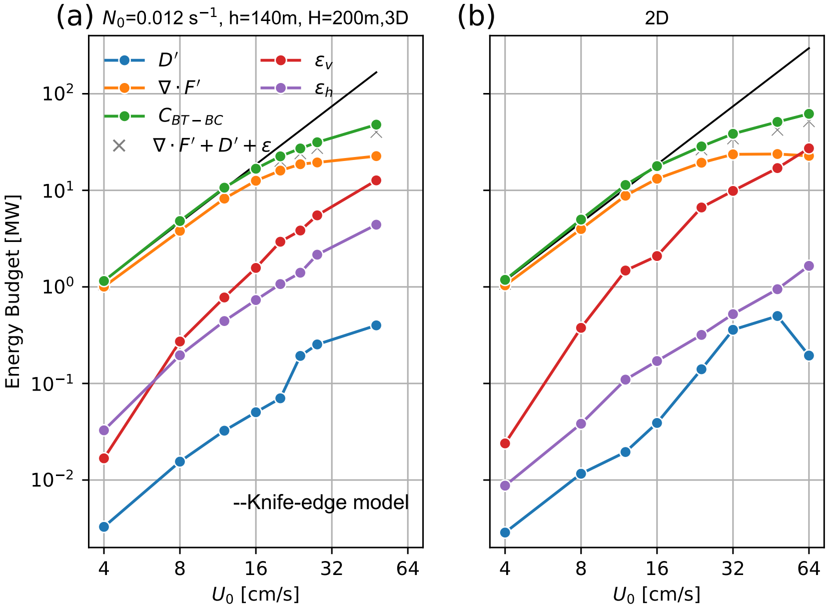

FIG. A1. Baroclinic energy budgets of the base run with $N_0 = 0.012$ s^{-1}, $h = 140$ m and $H = 200$ m, with colors representing different energy components as in FIG. 6, from (a) 3D simulations and (b) 2D simulations, which is the same with FIG. 6a.

APPENDIX B

Baroclinic Energy Budgets over all 2D simulations

This appendix provides an overview of the baroclinic energy budget from our suite of experiments. The upper panels display a series of experiments with varying ridge heights compared to the base run, while the lower panels depict variations in stratification relative to the base run. Each subplot encapsulates the detailed energetics corresponding to varying tidal forcing U_0 in each experiment. Notably, a saturation of energy conversion is observed consistently throughout all experiments.

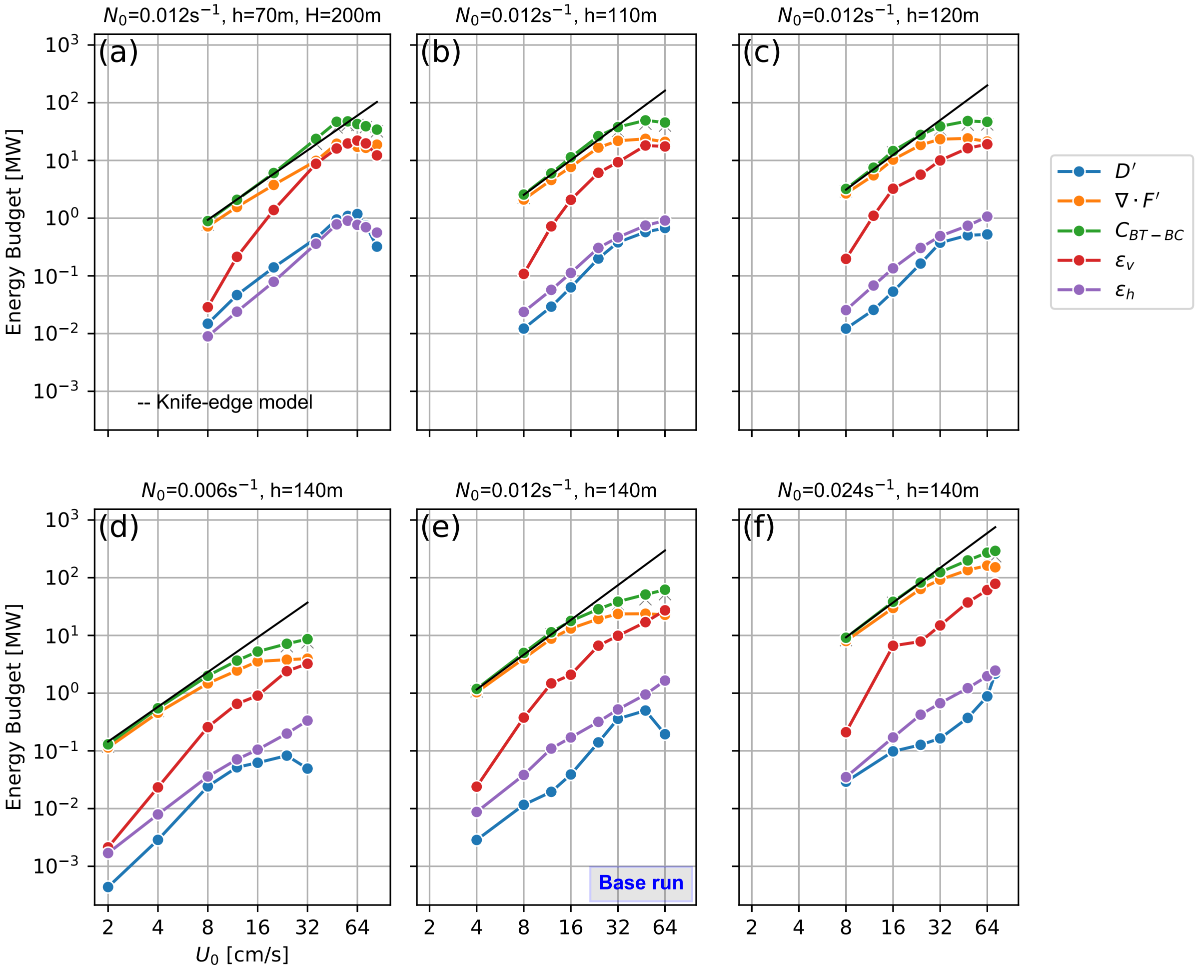

FIG. B1. Baroclinic energy budgets for the base run with (e) $N_0 = 0.012$ s^{-1} and $h = 140$ m and a series of experiments changing h, where (a) $h = 70$ m, (b) $h = 110$ m, (c) $h = 120$ m; and a series of experiments changing N_0, where (d) $N_0 = 0.006$ s^{-1}, and (f) $N_0 = 0.024$ s^{-1}. The colors indicating different energy components are the same as those used in FIG. 6. Knife-edge model for each experiment are shown in black lines.

References

Alford, M. H., and Coauthors, 2011: Energy flux and dissipation in luzon strait: Two tales of two ridges. *J. Phys. Oceanogr.*, **41 (11)**, 2211–2222, https://doi.org/10.1175/jpo-d-11-073.1.

Alford, M. H., and Coauthors, 2015: The formation and fate of internal waves in the south china sea. *Nature*, **521 (7550)**, 65–69, https://doi.org/10.1038/nature14399.

Arbic, B. K., S. T. Garner, R. W. Hallberg, and H. L. Simmons, 2004: The accuracy of surface elevations in forward global barotropic and baroclinic tide models. *Deep Sea Res. I*, **51 (25–26)**, 3069–3101, https://doi.org/10.1016/j.dsr2.2004.09.014.

Arbic, B. K., and R. B. Scott, 2008: On quadratic bottom drag, geostrophic turbulence, and oceanic mesoscale eddies. *J. Phys. Oceanogr.*, **38 (1)**, 84–103, https://doi.org/10.1175/2007jpo3653.1.

Armi, L., 1986: The hydraulics of two flowing layers with different densities. *J. Fluid Mech.*, **163**, 27–58, https://doi.org/10.1017/S0022112086002197.

Arneborg, L., P. Jansson, A. Staalstrøm, and G. Broström, 2017: Tidal energy loss, internal tide radiation, and local dissipation for two-layer tidal flow over a sill. *J. Phys. Oceanogr.*, **47 (7)**, 1521–1538, https://doi.org/10.1175/JPO-D-16-0148.1.

Baines, P., 1982: On internal tide generation models. *Deep Sea Res.*, **29 (3)**, 307–338, https://doi.org/10.1016/0198-0149(82)90098-x.

Baines, P. G., and K. P. Hoinka, 1985: Stratified flow over two-dimensional topography in fluid of infinite depth: A laboratory simulation. *J. Atmos. Sci.*, **42 (15)**, 1614–1630, https://doi.org/10.1175/1520-0469(1985)042⟨1614:sfotdt⟩2.0.co;2.

Bell, T. H., 1975: Lee waves in stratified flows with simple harmonic time dependence. *J. Fluid Mech.*, **67 (4)**, 705–722, https://doi.org/10.1017/S0022112075000560.

Bindoff, N. L., and Coauthors, 2019: Changing ocean, marine ecosystems, and dependent communities. *IPCC Special Report on the Ocean and Cryosphere in a Changing Climate*, Intergovernmental Panel on Climate Change, Switzerland, 477–587, URL https://eprints.qut.edu.au/206805/.

Blakely, C. P., and Coauthors, 2022: Dissipation and bathymetric sensitivities in an unstructured mesh global tidal model. *J. Geophys. Res.*, **127 (5)**, https://doi.org/10.1029/2021jc018178.

Bourgault, D., and D. E. Kelley, 2003: Wave-induced boundary mixing in a partially mixed estuary. *J. Mar. Res.*, **61 (5)**, 553–576, https://doi.org/10.1357/002224003771815954.

Buijsman, M., B. Arbic, J. Green, R. Helber, J. Richman, J. Shriver, P. Timko, and A. Wallcraft, 2015: Optimizing internal wave drag in a forward barotropic model with semidiurnal tides. *Ocean Modell.*, **85**, 42–55, https://doi.org/10.1016/j.ocemod.2014.11.003.

Carter, G. S., and Coauthors, 2008: Energetics of m2 barotropic-to-baroclinic tidal conversion at the hawaiian islands. *J. Phys. Oceanogr.*, **38 (10)**, 2205–2223, https://doi.org/10.1175/2008jpo3860.1.

Cummins, P. F., L. Armi, and S. Vagle, 2006: Upstream internal hydraulic jumps. *J. Phys. Oceanogr.*, **36 (5)**, 753–769, https://doi.org/10.1175/JPO2894.1.

Cummins, P. F., S. Vagle, L. Armi, and D. M. Farmer, 2003: Stratified flow over topography: upstream influence and generation of nonlinear internal waves. *Proc. Roy. Soc. London A*, **459 (2034)**, 1467–1487, https://doi.org/10.1098/rspa.2002.1077.

Egbert, G. D., and R. D. Ray, 2000: Significant dissipation of tidal energy in the deep ocean inferred from satellite altimeter data. *Nature*, **405 (6788)**, 775–778, https://doi.org/10.1038/35015531.

Egbert, G. D., and R. D. Ray, 2001: Estimates of m2 tidal energy dissipation from topex/poseidon altimeter data. *J. Geophys. Res.*, **106 (C10)**, 22 475–22 502, https://doi.org/10.1029/2000JC000699.

Egbert, G. D., R. D. Ray, and B. G. Bills, 2004: Numerical modeling of the global semidiurnal tide in the present day and in the last glacial maximum. *J. Geophys. Res.*, **109 (C3)**, https://doi.org/10.1029/2003jc001973.

Farmer, D., and L. Armi, 1999: Stratified flow over topography: the role of small-scale entrainment and mixing in flow establishment. *Proc. Roy. Soc. London A*, **455 (1989)**, 3221–3258, https://doi.org/10.1098/rspa.1999.0448.

Farmer, D. M., and R. A. Denton, 1985: Hydraulic control of flow over the sill in observatory inlet. *J. Geophys. Res.*, **90 (C5)**, 9051–9068, https://doi.org/10.1029/JC090iC05p09051.

Farmer, D. M., and H. J. Freeland, 1983: The physical oceanography of fjords. *Prog. Oceanogr.*, **12 (2)**, 147 – 219, https://doi.org/10.1016/0079-6611(83)90004-6.

Farmer, D. M., and J. D. Smith, 1980: Tidal interaction of stratified flow with a sill in knight inlet. *Deep Sea Res.*, **27 (3)**, 239–254, https://doi.org/10.1016/0198-0149(80)90015-1.

Green, J. A. M., and J. Nycander, 2013: A comparison of tidal conversion parameterizations for tidal models. *J. Phys. Oceanogr.*, **43 (1)**, 104–119, https://doi.org/10.1175/jpo-d-12-023.1.

Griffiths, S. D., and W. R. Peltier, 2009: Modeling of polar ocean tides at the last glacial maximum: Amplification, sensitivity, and climatological implications. *J. Climate*, **22 (11)**, 2905–2924, https://doi.org/10.1175/2008jcli2540.1.

Hughes, K. G., and J. M. Klymak, 2019: Tidal Conversion and Dissipation at Steep Topography in a Channel Poleward of the Critical Latitude. *J. Phys. Oceanogr.*, **49 (5)**, 1269–1291, https://doi.org/10.1175/JPO-D-18-0132.1.

Inall, M., F. Cottier, C. Griffiths, and T. Rippeth, 2004: Sill dynamics and energy transformation in a jet fjord. *Ocean Dyn.*, **54 (3)**, 307–314, https://doi.org/10.1007/s10236-003-0059-2.

Inall, M., T. Rippeth, C. Griffiths, and P. Wiles, 2005: Evolution and distribution of tke production and dissipation within stratified flow over topography. *Geophys. Res. Lett.*, **32 (8)**, https://doi.org/10.1029/2004GL022289.

Jayne, S. R., and L. C. S. Laurent, 2001: Parameterizing tidal dissipation over rough topography. *Geophys. Res. Lett.*, **28 (5)**, 811–814, https://doi.org/10.1029/2000gl012044.

Kang, D., 2011: Energetics and dynamics of internal tides in monterey bay using numerical simulations. Ph.D. thesis, Stanford University.

Kang, D., and O. Fringer, 2012: Energetics of barotropic and baroclinic tides in the monterey bay area. *J. Phys. Oceanogr.*, **42 (2)**, 272–290, https://doi.org/10.1175/JPO-D-11-039.1.

Kelly, S. M., J. D. Nash, and E. Kunze, 2010: Internal-tide energy over topography. *J. Geophys. Res.*, **115 (C6)**, https://doi.org/10.1029/2009JC005618.

Khatiwala, S., 2003: Generation of internal tides in an ocean of finite depth: analytical and numerical calculations. *Deep Sea Res. I*, **50 (1)**, 3–21, https://doi.org/10.1016/s0967-0637(02)00132-2.

Klymak, J. M., and M. C. Gregg, 2003: The role of upstream waves and a downstream density pool in the growth of lee waves: Stratified flow over the knight inlet sill. *J. Phys. Oceanogr.*, **33 (7)**, 1446–1461, https://doi.org/10.1175/1520-0485(2003)033⟨1446:trouwa⟩2.0.co;2.

Klymak, J. M., and M. C. Gregg, 2004: Tidally generated turbulence over the knight inlet sill. *J. Phys. Oceanogr.*, **34 (5)**, 1135–1151, https://doi.org/10.1175/1520-0485(2004)034⟨1135:tgtotk⟩2.0.co;2.

Klymak, J. M., S. Legg, and R. Pinkel, 2010a: A simple parameterization of turbulent tidal mixing near supercritical topography. *J. Phys. Oceanogr.*, **40 (9)**, 2059–2074, https://doi.org/10.1175/2010jpo4396.1.

Klymak, J. M., and S. M. Legg, 2010: A simple mixing scheme for models that resolve breaking internal waves. *Ocean Modell.*, **33 (3-4)**, 224–234, https://doi.org/10.1016/j.ocemod.2010.02.005.

Klymak, J. M., S. M. Legg, and R. Pinkel, 2010b: High-mode stationary waves in stratified flow over large obstacles. *J. Fluid Mech.*, **644**, 321–336, https://doi.org/10.1017/S0022112009992503.

Klymak, J. M., R. Pinkel, and L. Rainville, 2008: Direct breaking of the internal tide near topography: Kaena ridge, hawaii. *J. Phys. Oceanogr.*, **38 (2)**, 380–399, https://doi.org/10.1175/2007jpo3728.1.

Klymak, J. M., H. L. Simmons, D. Braznikov, S. Kelly, J. A. MacKinnon, M. H. Alford, R. Pinkel, and J. D. Nash, 2016: Reflection of linear internal tides from realistic topography: The tasman continental slope. *J. Phys. Oceanogr.*, **46 (11)**, 3321–3337, https://doi.org/10.1175/JPO-D-16-0061.1.

Klymak, J. M., and Coauthors, 2006: An estimate of tidal energy lost to turbulence at the hawaiian ridge. *J. Phys. Oceanogr.*, **36 (6)**, 1148–1164, https://doi.org/10.1175/JPO2885.1.

Lawrence, G. A., 1993: The hydraulics of steady two-layer flow over a fixed obstacle. *J. Fluid Mech.*, **254**, 605–633, https://doi.org/10.1017/S0022112093002277.

Legg, S., 2021: Mixing by oceanic lee waves. *Ann. Rev. Fluid Mech.*, **53 (1)**, 173–201, https://doi.org/10.1146/annurev-fluid-051220-043904.

Legg, S., and J. Klymak, 2008: Internal hydraulic jumps and overturning generated by tidal flow over a tall steep ridge. *J. Phys. Oceanogr.*, **38 (9)**, 1949–1964, https://doi.org/10.1175/2008jpo3777.1.

Llewellyn Smith, S. G., and W. R. Young, 2003: Tidal conversion at a very steep ridge. *J. Fluid Mech.*, **495**, 175–191, https://doi.org/10.1017/S0022112003006098.

Marshall, J., A. Adcroft, C. Hill, L. Perelman, and C. Heisey, 1997: A finite-volume, incompressible navier stokes model for studies of the ocean on parallel computers. *J. Geophys. Res.*, **102 (C3)**, 5753–5766, https://doi.org/10.1029/96jc02775.

Melet, A., M. Nikurashin, C. Muller, S. Falahat, J. Nycander, P. G. Timko, B. K. Arbic, and J. A. Goff, 2013: Internal tide generation by abyssal hills using analytical theory. *J. Geophys. Res.*, **118 (11)**, 6303–6318, https://doi.org/10.1002/2013jc009212.

Murray, S. P., A. Hecht, and A. Babcock., 1984: On the mean flow in the tiran strait in winter. *J. Mar. Res.*, **42 (2)**, 265–287, URL https://elischolar.library.yale.edu/journal_of_marine_research/1719.

Musgrave, R. C., J. A. MacKinnon, R. Pinkel, A. F. Waterhouse, and J. Nash, 2016: Tidally driven processes leading to near-field turbulence in a channel at the crest of the mendocino escarpment. *J. Phys. Oceanogr.*, **46 (4)**, 1137–1155, https://doi.org/10.1175/jpo-d-15-0021.1.

Musgrave, R. C., J. A. MacKinnon, R. Pinkel, A. F. Waterhouse, J. Nash, and S. M. Kelly, 2017: The influence of subinertial internal tides on near-topographic turbulence at the mendocino ridge: Observations and modeling. *J. Phys. Oceanogr.*, **47 (8)**, 2139–2154, https://doi.org/10.1175/jpo-d-16-0278.1.

New, A., K. Dyer, and R. Lewis, 1987: Internal waves and intense mixing periods in a partially stratified estuary. *Estuar. Coast. Shelf Sci.*, **24 (1)**, 15–33, https://doi.org/10.1016/0272-7714(87)90003-5.

Nikurashin, M., and R. Ferrari, 2010: Radiation and dissipation of internal waves generated by geostrophic motions impinging on small-scale topography: Theory. *J. Phys. Oceanogr.*, **40 (5)**, 1055–1074, https://doi.org/10.1175/2009jpo4199.1.

Simmons, H. L., R. W. Hallberg, and B. K. Arbic, 2004: Internal wave generation in a global baroclinic tide model. *Deep Sea Res. II*, **51 (25-26)**, 3043–3068, https://doi.org/10.1016/j.dsr2.2004.09.015.

St. Laurent, L., S. Stringer, C. Garrett, and D. Perrault-Joncas, 2003: The generation of internal tides at abrupt topography. *Deep Sea Res. I*, **50 (8)**, 987–1003, https://doi.org/10.1016/s0967-0637(03)00096-7.

St. Laurent, L. C., H. L. Simmons, and S. R. Jayne, 2002: Estimating tidally driven mixing in the deep ocean. *Geophys. Res. Lett.*, **29 (23)**, 21–1–21–4, https://doi.org/10.1029/2002gl015633.

Staalstrøm, A., E. Aas, and B. Liljebladh, 2012: Propagation and dissipation of internal tides in the oslofjord. *Ocean Sci.*, **8 (4)**, 525–543, https://doi.org/10.5194/os-8-525-2012.

Staalstrøm, A., L. Arneborg, B. Liljebladh, and G. Broström, 2015: Observations of turbulence caused by a combination of tides and mean baroclinic flow over a fjord sill. *J. Phys. Oceanogr.*, **45 (2)**, 355–368, https://doi.org/10.1175/JPO-D-13-0200.1.

Staalstrøm, A., and L. P. Røed, 2016: Vertical mixing and internal wave energy fluxes in a sill fjord. *J. Mar. Syst.*, **159**, 15–32, https://doi.org/10.1016/j.jmarsys.2016.02.005.

Stacey, M. W., 2005: Review of the partition of tidal energy in five canadian fjords. *J. Coast. Res.*, **21 (4 (214))**, 731–746, https://doi.org/10.2112/002-NIS.1.

Stammer, D., and Coauthors, 2014: Accuracy assessment of global barotropic ocean tide models. *Reviews of Geophysics*, **52 (3)**, 243–282, https://doi.org/10.1002/2014rg000450.

Stashchuk, N., M. E. Inall, and V. Vlasenko, 2007: Analysis of supercritical stratified tidal flow in a scottish fjord. *J. Phys. Oceanogr.*, **37**, 1793–1810, https://doi.org/10.1175/JPO3087.1.

Stigebrandt, A., 1976: Vertical diffusion driven by internal waves in a sill fjord. *J. Phys. Oceanogr.*, **6 (4)**, 486–495, https://doi.org/10.1175/1520-0485(1976)006⟨0486:vddbiw⟩2.0.co;2.

Stigebrandt, A., 2012: Hydrodynamics and circulation of fjords. *Encyclopedia of Lakes and Reservoirs*, L. Bengtsson, R. W. Herschy, and R. W. Fairbridge, Eds., Springer Netherlands, Dordrecht, 327–344, https://doi.org/10.1007/978-1-4020-4410-6{_}247.

Stigebrandt, A., and J. Aure, 1989: Vertical mixing in basin waters of fjords. *J. Phys. Oceanogr.*, **19 (7)**, 917–926, https://doi.org/10.1175/1520-0485(1989)019⟨0917:vmibwo⟩2.0.co;2.

Sulzbach, R., H. Dobslaw, and M. Thomas, 2021: High-resolution numerical modeling of barotropic global ocean tides for satellite gravimetry. *J. Geophys. Res.*, **126 (5)**, https://doi.org/10.1029/2020jc017097.

Voet, G., M. H. Alford, J. A. MacKinnon, and J. D. Nash, 2020: Topographic form drag on tides and low-frequency flow: Observations of nonlinear lee waves over a tall submarine ridge near palau. *J. Phys. Oceanogr.*, **50 (5)**, 1489–1507, https://doi.org/10.1175/JPO-D-19-0257.1.

Wang, D.-P., 2006: Tidally generated internal waves in partially mixed estuaries. *Cont. Shelf Res.*, **26 (12–13)**, 1469–1480, https://doi.org/10.1016/j.csr.2006.02.015.

Winters, K. B., and L. Armi, 2012: Hydraulic control of continuously stratified flow over an obstacle. *J. Fluid Mech.*, **700**, 502–513, https://doi.org/10.1017/jfm.2012.157.

Winters, K. B., and L. Armi, 2013: The response of a continuously stratified fluid to an oscillating flow past an obstacle. *J. Fluid Mech.*, **727**, 83–118, https://doi.org/10.1017/jfm.2013.247.